X-RAY MICROSCOPE PERFORMANCE ENHANCEMENT THROUGH CONTROL
ARCHITECTURE CHANGE

BY

SHEIKH TAMJID MASHRAFI

THESIS

Submitted in partial fulfillment of the requirements
for the degree of Master of Science in Mechanical Engineering
in the Graduate College of the
University of Illinois at Urbana-Champaign, 2013

Urbana, Illinois

Master's Committee:

      Professor Srinivasa M Salapaka, Chair
      Professor Curt Preissner

ABSTRACT

The goal of this thesis is to apply control algorithms to improve the performance of nanopositioning devices used on the beamline in Advanced Photon Source (APS) at Argonne National Laboratory (ANL). A prototype device, better known as the Early User Instrument (EUI) was the subject of this work. It consists of X-ray optics stage group that focuses the X-ray beam as a source-size-limited spot onto a sample held on the sample stage group. The controller algorithms that are used should provide the closed-loop with robust stability, large bandwidth, high resolution, disturbance rejection and noise attenuation. Conveniently, the field of scanning probe microscopes (SPMs) have already flourished on this aspect of controller algorithms proven to give desired closed-loop properties. Controller algorithms such as Proportional Integral Derivative (PID), Glover-McFarlane H_∞ algorithm, and 1DOF H_∞ controller were designed and implemented on the EUI system. The controller hardware used for implementation is National Instruments (NI) CompactRIO hardware that consists of a real-time controller, a FPGA built into the hardware chassis, analog I/O modules, and digital I/O modules. NI LabVIEW, the dedicated software to the NI hardware, was used to represent the discrete controllers as biquads structures that ran in the FPGA as a part of the closed-loop . The largest closed-loop bandwidth achieved is of 65 Hz through the 1DOF H_∞ controller and is a 171% improvement over the traditional PID controller. Highest closed-loop resolution achieved by the EUI with a 50 Hz bandwidth 1DOF H_∞ controller is 1.4 nanometers, which is a 180% improvement over the open loop resolution of 7 nanometers.

To my parents, for their love and support.

ACKNOWLEDGMENTS

I would like to thank my advisor, Dr. Srinivasa M. Salapaka for his patience, continuous guidance and encouragement throughout the years at UIUC. I would also like to thank my coadvisor Dr. Curt Preissner of Advanced Photon Source (APS) at Argonne National Laboratory (ANL) for his constructive advice and mentoring during my work at ANL.

Thanks to Allen Zhao of ANL for helping me with the LabVIEW coding for controller implementation and also for providing with the code that he wrote for the open loop implementation of EUI.

I would also like to express my gratitude to my research colleague Dr. Gayathri Mohan for helping in starting through the beginning years at UIUC and showing me the atomic force microscope details. Also would like to thank my other research colleagues Yunwen Xu, Ram Sai Gorugantu, and Mayank Baranwal.

I would like to show my sincere gratitude to Dr. Zubaer Hossain for showing me the path from the begining of my graduate study at UIUC. I would also like to thank my friends, specially Shama Farabi Barna, Chowdhury Mahbub Ashraf and Piyas Bal Chowdhury for their support.

Thanks to my parents and my elder sibling for their love and support. This truly is the force that keeps me going.

TABLE OF CONTENTS

LIST OF FIGURES

LIST OF ABBREVIATIONS

APS   Advanced Photon Source

ANL   Argonne National Laboratory

CPSD   Cross Power Spectral Density

DOF   Degree Of Freedom

DTFT   Discrete-Time Fourier Transform

EUI   Early User Instrument

FPGA   Field Programmable Gate Array

HDL   Hardware Description Language

HLS   High-Level Synthesis

HXN   Hard X-ray Nanoprobe

ISN   In Situ Nanoprobe

LDDM   Laser Doppler Displacement Meter

LHP   Left Half Plane

NI   National Instruments

PI   Physik Instrumente

PSD   Power Spectral Density

RHP   Right Half Plane

RIO   Reconfigurable Input/Output

SPM   Scanning Probe Microscope

CHAPTER 1

INTRODUCTION

This thesis presents control design to improve the performance of a X-ray nanopositioning system used at the Advanced Photon Source (APS) at Argonne National Laboratory (ANL). The nanopositioning system known as the Early User Instrument (EUI) is used on the beamline to focus the X-ray beam through focusing optics on to a sample. The device design is based on the prototype for the hard X-ray nanoprobe (HXN) [6, 9]. This instrument developed in 2004 was primarily used to test the nanoprobe basic instrument design and preliminary imaging studies. Now the EUI is used as a testbed for the work in this thesis. More specifically, the EUI optics stage precisely positions the X-ray optical apparatus so that it can focus the X-ray beam on to the sample held on a sample holder on top of the sample stage. The image resolution depends on how accurate the lateral relative position of zone plate optics and sample is maintained. In earlier experiments on an APS beamline, EUI achieved a source-size-limited focal spot of 70 nm [9]. In this thesis, we present a framework to model, analyze, and control precision positioning stages. The main goals of the control design are to achieve high position tracking bandwidth, resolution, and robustness to modeling and environmental uncertainties. Even though we demonstrate the framework on an EUI positioning system, it is general to accommodate different positioning systems that are being used (and planned to be later used) on the APS beamline.

Current X-ray microscopes such as HXN at the APS can focus the X-rays to a 30 nm spot size [3]. The HXN is based on combination of scanning probe and full-field imaging microscopy and typically used for fluorescence mapping, nanodiffraction and transmission imaging. It is expected that new microscopes such as the in situ nanoprobe (ISN) will focus X-rays to a 20 nm spot size [2]. In case of EUI, only the traditional Proportional Integral Derivative (PID) controllers were implemented using a group of CS900 rack-mount industrial PC-computers running WINDOWS 2000 operating system and standard National Instruments (NI) LabVIEW software [9]. The PID controller design does not offer flexibility in design, robust stability property, high bandwidth and high resolution.

This work exploits the control design tools developed for positioning systems in scanning probe microscopy (SPM) and applies them to positioning systems on the APS beamline. In

context of SPM, there has been a significant development of control architecture, which have resulted in large improvements in robust stability, bandwidth, and resolution of nanopositioning systems. For instance, Glover-McFarlane control design [8, 12] has resulted in greater reliability and repeatability of positioning systems. In this design, an add-on controller block is implemented in addition to an existing controller; the resulting closed loop system is insensitive (robust) to modeling uncertainties such as parametric uncertainties, floor and environment disturbances, and sensor noise. This robustness to uncertainties comes at a relatively small compromise of device performance (this compromise is quantifiable a priori). This design is especially useful for wrapping around existing control designs that give good performance (such as tracking bandwidth) but are sensitive to modeling uncertainties (such as floor vibrations). 1 DOF H_∞ control design [8, 10] provides a framework for designing the control from scratch. It gives the flexibility of quantifying trade-offs between performance objectives, assess if the desired specifications are feasible and provides with a controller algorithm that satisfies the specifications as closely as possible. Although not used in this work, another design methodology that combines the feedforward and feedback techniques - the 2 DOF H_∞ controller algorithm [4]. Since, the 2 DOF controller algorithm is based on *both* the reference and measured plant output signal in contrast to *only* their difference in 1DOF designs, it achieves better robustness and performance objectives.

Although the SPMs are smaller in size compared to X-ray microscopes the controller design methodologies proved worthy for SPMs do apply to the later microscopes. So, the already developed control architecture in SPM community was applied to the X-ray microscope at hand, that is the EUI system to improve the performance. The X-ray microscope used in United States and the world are room-sized devices that consists of many components and bound by numerous constraints. The nanopositioning system is only one component of the X-ray microscope. With such a complex and integrated system any physical change to the nanopositioning mechanics requires a significant investment in effort and money. Also any change might have a cascade effect on the other components of the microscope. So, changing only the control architecture is a cost effective way to improve the performance.

This thesis shows the design and implementation of PID algorithm and two other algorithms namely the Glover-McFarlane, and 1 DOF H_∞ design that are used for the first time in X-ray nanopositioning devices as EUI. In addition, the control hardware which is the National Instruments (NI) CompactRIO hardware is also combined with EUI(or similar X-ray nanopositioning devices) for the first time. The control architecture that was applied improves the performance of the nanopositioning system by giving a 171% improvement of bandwidth from PID controller to a 1DOF H_∞ controller. There was 180% improvement of resolution from a 50 Hz bandwidth 1 DOF H_∞ controller when compared to the open loop

resolution. Both improvement in bandwidth and resolution are solely due to implementing new control algorithm on a new hardware. The higher X-ray resolution achieved by this approach enhances the microscope stability during the operations in which stability is critical such as X-ray fluorescence mapping. The higher bandwidth achieved can make it possible to scan large area optimally.

Improvements of the EUI, a prototype of the APS nanoprobe, would mean that the controller algorithms will be readily and effectively applicable to the Hard X-ray nanoprobe and other similar X-ray nanopositioning devices used in other light sources around the world. The APS users, beamline scientists, and researchers coming from all around the world would benefit from higher imaging resolution and bandwidth. Novel research and scientific experiments might be possible with this added capability of the nanoprobe hardware.

This thesis is organized as follows. The system details of the EUI, the layout of closed-loop system with the new NI hardware, system identification of the fine Y-stage, model fitting, and model reduction are given in the chapter-2. Chapter-3 showcases the pure feedback controllers as PID, Glover-McFarlane H_∞ design and the 1 DOF H_∞ controller. The theoretical details, some design specifications and implementation details are emphasized in this section. The last chapter concludes the whole work and directs towards the things that needs to be done in the future.

CHAPTER 2

EUI SYSTEM

2.1 Device Description

The nanopositioning device for which controller algorithm is developed is named EUI, which is a prototype of the APS hard X-ray nanoprobe instrument. EUI was developed in 2004 by the APS at ANL. APS is a third-generation synchrotron radiation source that generates high-brilliance x-ray beams and provides powerful tools for basic science and applied research in the fields of physics, life science, materials science, environmental science, and chemistry. EUI is the acting testbed for design and implementation of controllers to achieve larger bandwidth, higher resolution, disturbance rejection and noise attenuation.
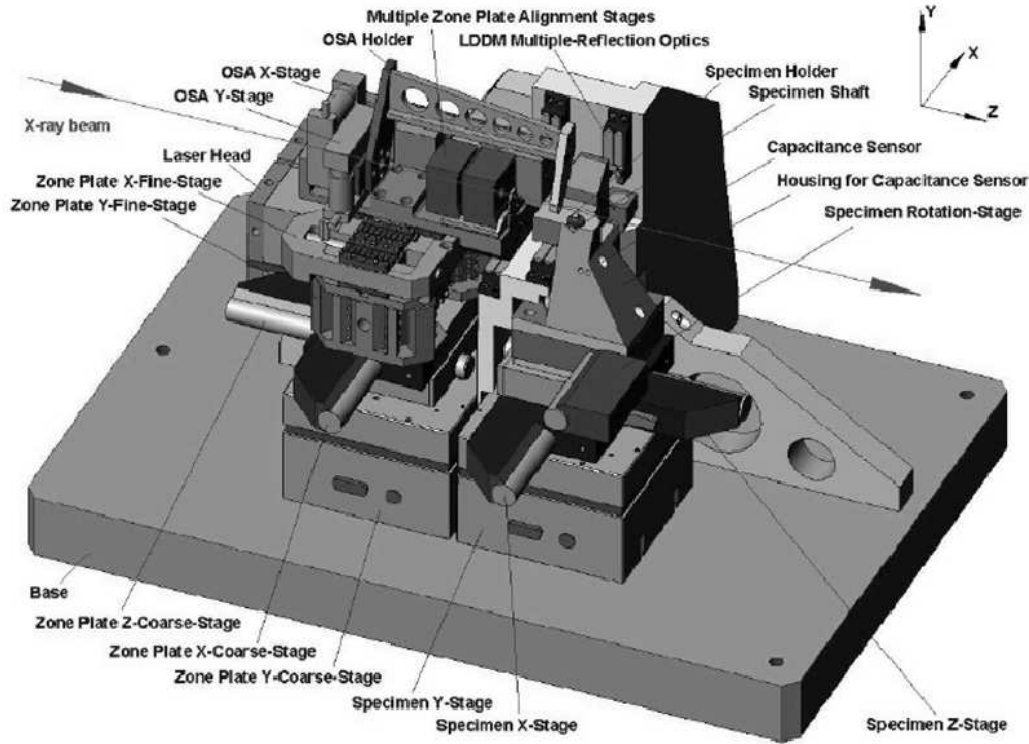
Figure 2.1: A 3D model of the EUI, a prototype nanoprobe with high-resolution weak-link stages, image from reference [9].

The EUI consists of three major components groups: a supporting base, a X-ray zone plate optics stage group, and a specimen or sample holders stage group, as shown in Figure 2.1. The zone plate optics stage group consists of custom flexure stages driven by piezoelectric actuators stacks and is used for the purpose of all high-precision positioning and scanning. The specimen stage group is used only for coarse positioning. Zone plate stage group consists of 3 coarse stages: Z-coarse stage, Y-coarse stage, X-coarse stage, and 2 fine stages: Y-fine stage and X-fine stage. The three coarse optics stages are driven by commercial DC-motors and the two fine optics stages are piezoelectric-transducer (PZT) stack driven high-stiffness stages. Work in this thesis concentrates on zone plate Y-fine stage. Note, that Y-direction is the vertical direction.

A 2D differential laser Doppler displacement meter (LDDM) is used to measure the position of the stages. The EUI was designed to accommodate a multiple-reflection of the laser that improves the sensitivity and resolution of the encoding system. As a result the encoder system has a sub-nanometer resolution. The laser encoders are placed on the supporting base in a precise orientation to ensure alignment with the optics.
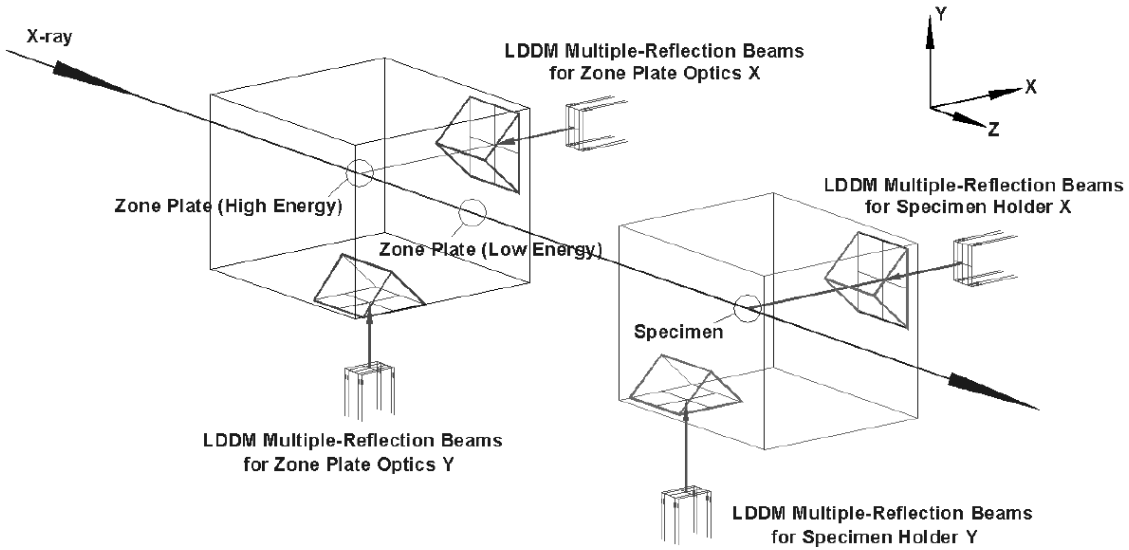
Figure 2.2: A configuration with four-LDDM encoder system for EUI optics stage group and specimen stage group, image from reference [9].

A group of LDDMs, multiple reflection laser optics and a reference frame makes up the encoder system of the EUI. The reference frame with respect to which all positions are measured defines the coordinate system of the EUI. In the Figure 2.2 it is seen the way the X-ray passes through the high-energy or low-energy zone-plates. Then this X-ray gets focused as a source-size-limited spot onto the specimen. In the above configuration four LDDM encoders are used for positioning the stages - two encoders for the zone-plate optics

stage and two for the sample stage. As shown in Figure 2.2, two LDDMs for EUI optics stage and two LDDMs for EUI sample stage are used to perform a 2D differential measurement between these stage groups.
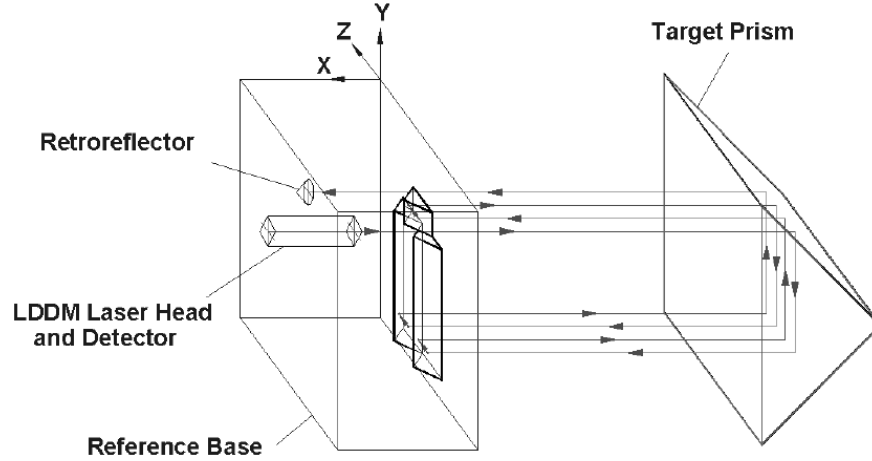
Figure 2.3: A schematic of the self-aligning multiple reflection laser optics design used in the EUI, image from reference [9].

The working principle of LDDM is based on the principles of the Doppler effect and optical heterodyning. The LDDMs used are custom-made by Optodyne, Inc. This LDDM has high resolution of around 2 nm, fast object speed of 2 m/s, and its performance is independent of polarization. Due to these characteristics designing a multiple reflection based optical design (Figure 2.3) to attain sub-nanometer resolution was possible. The heterodyning detector is housed co-axially inside the laser source. The laser beam is reflected back and forth eight times between the reference base and the moving target (Y-stage in this work) using precisely positioned optical prisms. The frequency-shifted laser beam is reflected back to the heterodyning detector. This optical path for laser results in eight times greater resolution for the linear displacement measurement and encoding when compared to single reflection of laser on a moving target.

2.2 System Setup

One of the steps of EUI fine positioning is the differential positioning in vertical (Y) direction. Two LDDMs are used to determine the vertical position of optics on the optics stage group and the sample at the sample stage group. The two stage groups need to be positioned precisely with respect to each other so that the focusing optics on the optics stage focuses a X-ray beam spot on the sample held on the sample stage group. The coordinate system is defined based on the supporting frame acting as a reference. The positioning of the fine Y-stage of the optics stage group is of primary interest in this thesis.

The original EUI control system consisted of a group of CS900 rack-mount industrial PC-computers running WINDOWS 2000 and National Instrument (NI) LABVIEW software. A PID controller was implemented on standard LABVIEW with limited bandwidth. The position of the Y-stages in the vertical direction were measured and sent back to industrial PCs where a PID controller operated in feedback loop. Then the controller output after passing though a digital to analog converter (DAC) would go to the piezo-stack controllers. The piezo-stack controllers would pass the corresponding voltage signals to the Physik Instrumente piezo-stacks, which acted as the actuators for the system. Thus eventually the position of the stages would have been corrected. Two things that limit the performance of the original system are the control hardware available and the controller algorithm (PID) used.
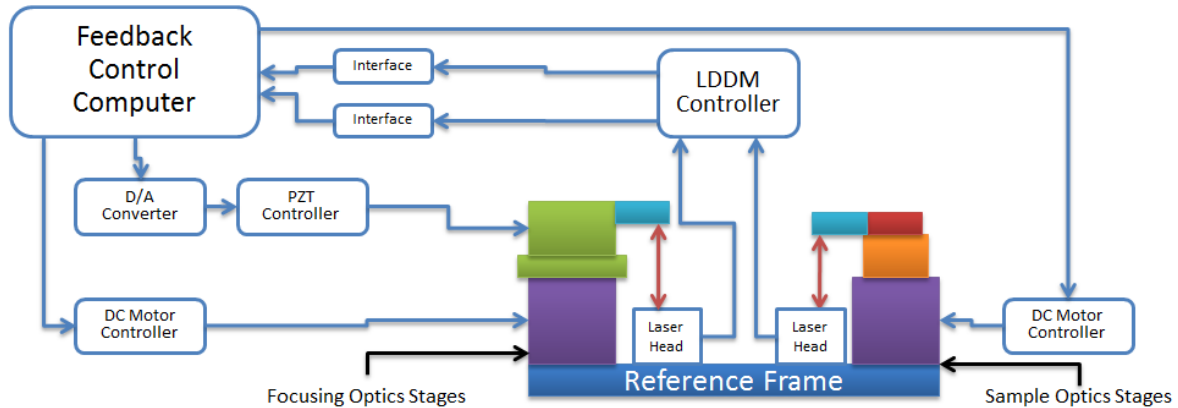
Figure 2.4: A schematic showing the system layout of EUI. The fine motion stage is part of the focusing optics stage group.

Present work shown here uses a new Field Programmable Gate Array (FPGA) based control hardware and new controller algorithm. The control hardware is National Instruments (NI) CompactRIO hardware consisting of cRIO-9024 real-time controller, cRIO-9118 Virtex-5 LX110 FPGA chassis, NI-9223 analog input modules, NI-9402 digital input modules, and

7

NI-9263 analog output modules. The NI FPGA based hardware acted as a capable platform for the high-end control architecture to be implemented. The FPGA in the reconfigurable input/output (RIO) architecture provided the flexibility to implement advanced custom control algorithm represented as biquads structure directly on the FPGA fabric. The Virtex-5 FPGA chip built in the CompactRIO chassis has a clock cycle of 40 MHz and is capable of running loops at a rate as high as 1 MHz. Running the controller directly in the FPGA fabric significantly increases the loop rate and minimizes the latency. Also the dedicated software for this hardware, NI LabVIEW, is a graphical high-level synthesis (HLS) design tool or language that makes it exceptionally easy to generate optimized hardware description language (HDL) for representing custom algorithms on the FPGA chip.

The new system layout is shown in Figure 2.4. As before the position of the optics fine Y-stage and specimen coarse Y-stage in the vertical direction are measured by the LDDMs. However, in the new system the signals are sent back through the NI-9223 analog input module to the FPGA that is in the NI CompactRIO chassis. Discrete feedback controller algorithms run directly on this Virtex-5 FPGA. The controller takes in the position error signal computed from the reference signal and the measured vertical position of the stages and generates a controller output (also known as system input). This system input goes through the NI-9263 analog output module, gets amplified by an amplifier before going to the piezo-stacks controller. The piezo-stack controllers pass the corresponding voltage signals to the Physik Instrumente (PI) piezo-stacks, which are the actuators for the system. This is the feedback loop for the closed-loop system for fine Y-stage.

2.3 System Identification

An accurate, bottom-up mathematical model of EUI fine Y-Stage based on laws of physics would be very hard to achieve given the complexity of the system. So an experimental approach was taken to model EUI dynamical system. The method is the well known black-box identification method where the system is modeled without looking into the internal structure or dynamics of the system. A signal is provided to the system and the output is measured. Everything in between the input signal and the output signal is considered as the black-box, of which nothing is known. A parametric or non-parametric model is fitted to this experimental input-output data.

The non-parametric system identification method that was applied here utilizes the Welch's method. Welch's method provides an estimator of the power spectral density (PSD) detailed in the paper by Welch [13]. This method divides a given time series data into segments (possibly overlapping), calculates the estimated PSD for each segmented data, and then averages this PSD estimates. The *pwelch* function in MATLAB conveniently gives PSD estimates using this method. The PSD estimate on each segment is nothing but calculating the discrete-time Fourier transform (DTFT) of the samples in the data and then scaling the magnitude squared of the DTFT.

Suppose, fine Y-stage G_y is a linear, time invariant system and $x(n)$ and $y(n)$ are the input and output time-domain data of the system respectively. The power spectrum of $x(n)$ and cross spectral density (CPSD) of $x(n)$ and $y(n)$ are related as follows:

$$P_{yx}(\omega) \,=\, G_y(\omega)\,P_{xx}(\omega), \tag{2.1}$$

Where P_{xx} = power spectral density of the input signal x,
P_{yx} = cross power spectral density of the input signal x and output y

$$G_y(\omega) \,=\, \frac{P_{yx}(\omega)}{P_{xx}(\omega)} \tag{2.2}$$

Here, G_y is the non-parametric transfer function estimate of the actual system by Welch's method. MATLAB function *tfestimate* calculates this transfer function estimate, utilizing the Welch's method of estimating PSD from a given input and output time domain data. Moreover, *tfestimate* estimates both magnitude and phase information of the actual system.

In this particular case the EUI system is excited with band-limited uniform Gaussian white noise of a specific amplitude. A band-limited Gaussian white noise from 0 to 12.5 kHz was chosen so as to not excite the system with any higher frequency components. High

9

frequency content can excite nonlinearities and also reduce the excitation energy in the band of interest. The output of the system is measured for a certain time period. Then a non-parametric transfer function model was calculated from this input-output data using the *tfestimate* function. To obtain a parametric transfer function model a curve fitting was done using the MATLAB function *invfreqs*. Verification of the obtained model is performed (detailed in section 2.0.6) to make sure that it represents the actual system properly.
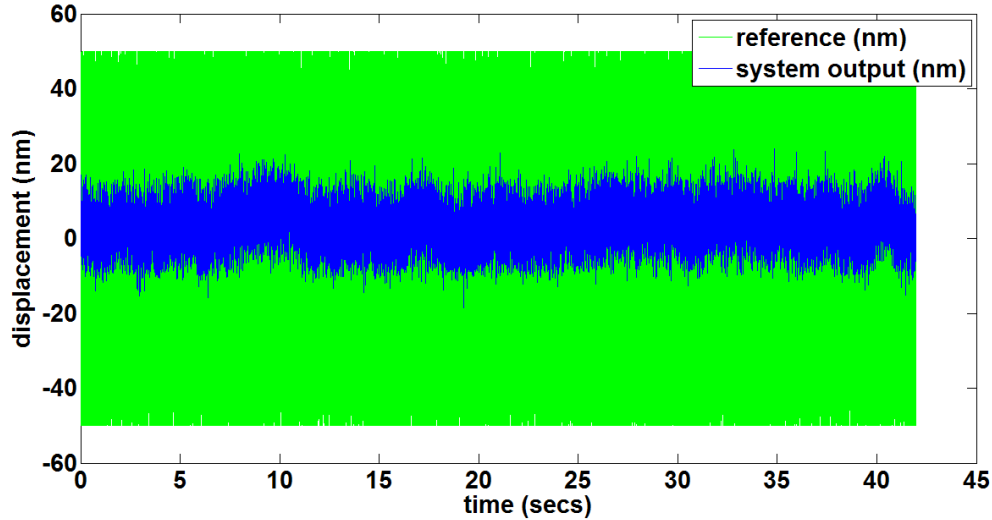
Figure 2.5: 50 nm amplitude uniform white noise as reference (in green) input to the system and measured system output (in blue).

To investigate how the experimental model varies with amplitude, the amplitude of the input data or the uniform white noise was varied between 50 nm, 200 nm, 500 nm and 1000 nm. The maximum safe operating displacement from zero of the fine Y-stage is limited to 2000 nanometers. The usual operating amplitude might be around few hundreds of nanometers. Ten data sets were collected for each of the amplitudes 50 nm, 200 nm, 500 nm, and 1000 nm. Then 40 non-parametric transfer function estimates were calculated for the 40 different data shown the Figure 2.6. A voltage signal was given as input to the system and the output measured as nanometers of displacement of the fine stage Y. Hence, the magnitude of the nonparametric transfer function estimate is in nm/V unit.

Then the 10 sets of calculated transfer function estimated data corresponding to a particular amplitude (say of 50 nm uniform white noise) were averaged. This resulted into four averaged non-parametric transfer function estimates corresponding to four different amplitudes, as shown in the Figure 2.7. The system exhibits a softening non-linearity. That is, as the amplitude of the input white noise is increased from 50 nm to 1000 nm the resonance peak moved towards lower frequency. The exact reason for this is unknown, though it may be related to the flexure design on the stage.
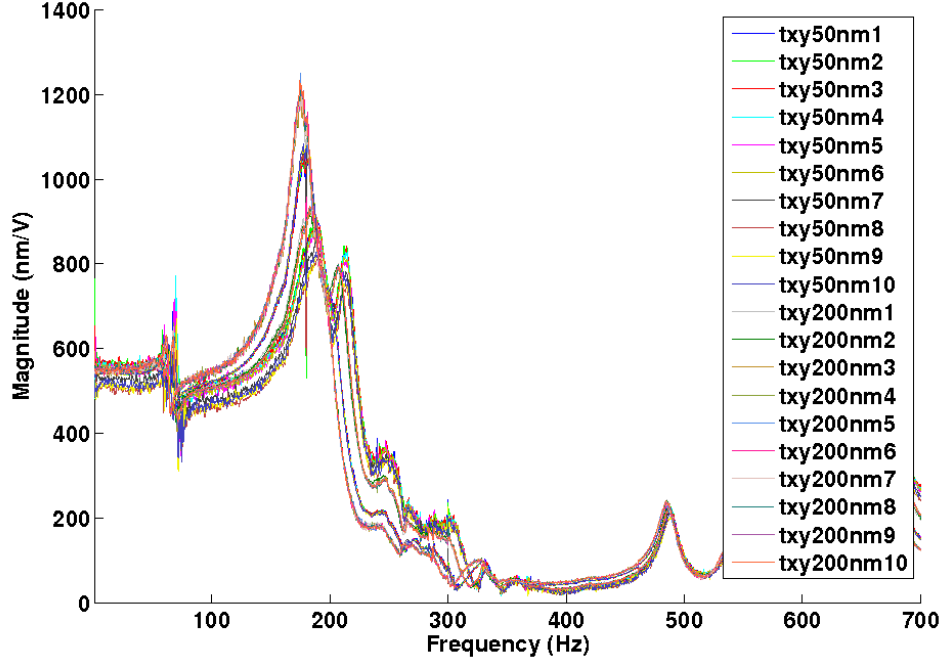
Figure 2.6: 40 different non-parametric transfer function estimates calculated by Welch's method. There are four groups of data for 50 nm, 200 nm, 500 nm, 1000 nm input white noise amplitudes, with each group containing 10 sets of data.
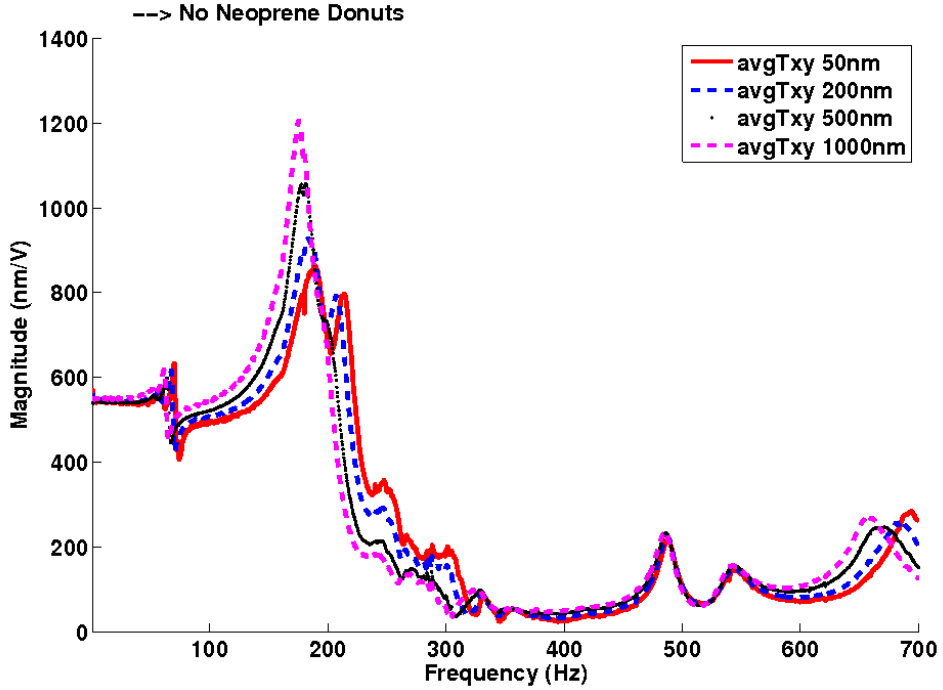
Figure 2.7: Averaged non-parametric transfer functions of the fine Y-stage for 50 nm, 200 nm, 500 nm, 1000 nm input white noise amplitudes. The system exhibits a softening non-linearity.

2.4 Model Fitting

The calculated experimental frequency response of the fine Y-stage is a non-parametric model. So, a parametric model is fitted to this non-parametric model using a curve-fitting process. Then using the parameters of this fitted model a transfer function model of the Y-stage is achieved. In Figure 2.8 it is clear that the fitted model captures the significant peaks of the experimental frequency response. The resonant peak of the plant is at 188 Hz (1182 rad/s). That is, the open loop bandwidth of Y-stage is 188 Hz. Note that the frequency range of the interest so as to capture plant characteristics that are significant for control implementation on the EUI is 0 to 250 Hz (1570 rad/s). Although in operation frequency over the open loop bandwidth will not be used.
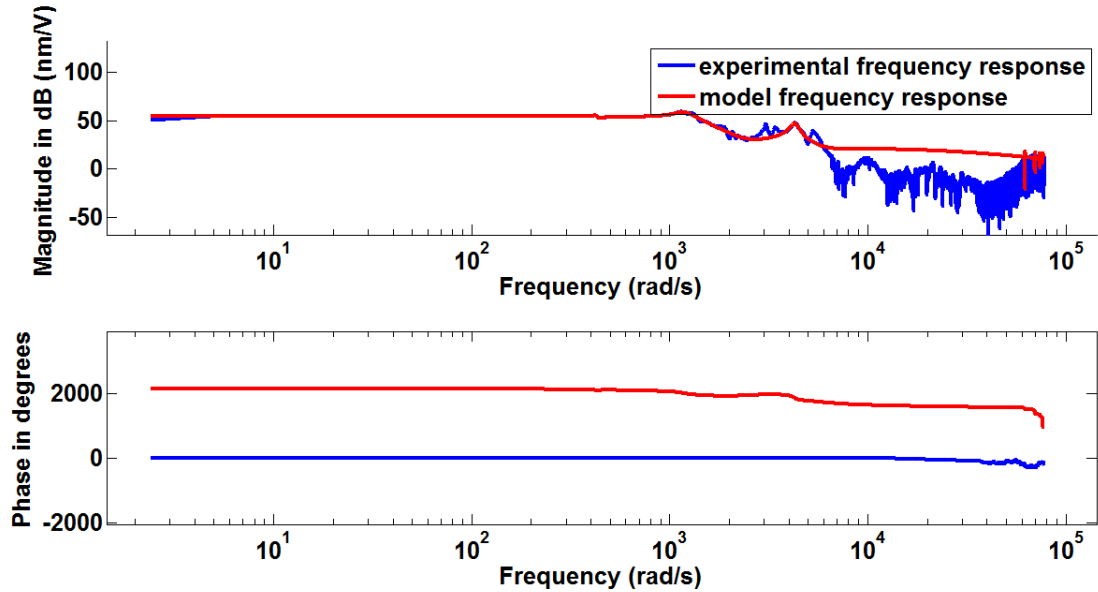
Figure 2.8: Fitting a transfer function model to the experimental frequency response calculation.

As given below Gy is the 21st order transfer function model of the fine Y-stage of the optics stage group.

$$Gy = \frac{numtf}{dentf} \tag{2.3}$$

$$numtf = -3.04e22s^{19} - 7.591e27s^{18} - 5.662e32s^{17} - 1.529e38s^{16} - 3.696e42s^{15}$$
$$- 1.149e48s^{14} - 8.688e51s^{13} - 3.822e57s^{12} + 2.181e60s^{11} - 4.801e66s^{10}$$
$$+ 2.512e70s^{9} - 2.135e74s^{8} + 5.041e77s^{7} - 7.343e80s^{6} + 4.671e84s^{5}$$
$$+ 1.295e87s^{4} + 6.718e90s^{3} + 9.75e92s^{2} + 1.127e96s + 1.157e98$$

$$dentf = s^{21} + 1.017e15s^{20} + 2.749e22s^{19} + 6.717e26s^{18} + 5.563e32s^{17} + 1.32e37s^{16}$$
$$+ 4.199e42s^{15} + 9.792e46s^{14} + 1.406e52s^{13} + 3.222e56s^{12} + 1.787e61s^{11}$$
$$+ 3.979e65s^{10} + 1.121e69s^{9} + 8.939e72s^{8} + 1.479e76s^{7} + 3.104e79s^{6}$$
$$+ 3.154e82s^{5} + 3.023e85s^{4} + 1.864e88s^{3} + 5.994e90s^{2} + 2.443e93s$$
$$+ 2.202e95$$

2.5 Balance Realization and Model Reduction

A state space realization that has its controllability and observability grammians equal and diagonal, is called a balanced realization [15]. It can be assumed that the fine Y-stage plant G_y has a state-space realization of (A, B, C, D). This state-space realization is called a minimal realization if (C, A) is observable and (A, B) is controllable. Minimal realization is the lowest order realization possible for a given system. The A matrix of the minimal realization is Hurwitz. To obtain a balance realization of a system, it is usual practice to start with the minimal realization of the system and apply a certain state transformation. When the system is balanced the controllability and the observability ellipsoids are exactly aligned. Thus the states which are most controllable are also most observable. Balance realization usually comes as a precursor step of model reduction.
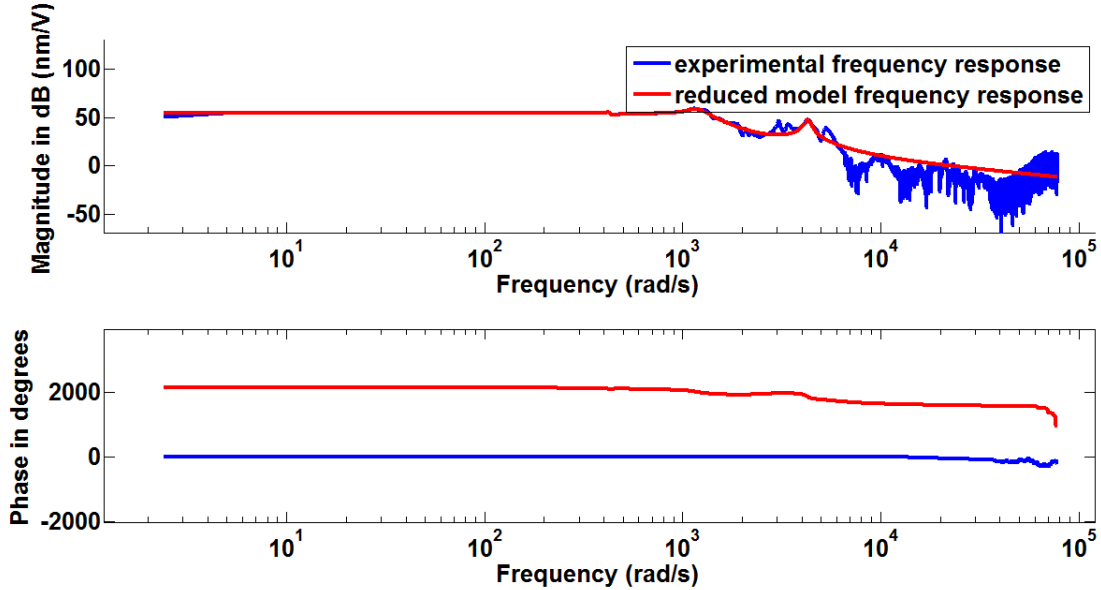
Figure 2.9: Experimental Frequency response and reduced fitted transfer function model of fine Y-stage.

In the model reduction step the states that are most controllable and most observable are preserved, while the least observable and controllable states are eliminated. Through balance realization the Hankel singular values are oriented from large to small, with the interpretation that the states corresponding to large Hankel singular values are strongly controllable and observable. So, by balanced truncation technique the states with small Hankel singular values are truncated. While following this process of model reduction it is important to keep the system input-output properties approximately same.

In this particular case, the reduced model, rGy of the fine Y-stage is a 9th order transfer

function. This reduced model clearly fits the experimental frequency response well up to approximately 4200 rad/s shown in Figure 2.9.

$$rGy = \frac{rnumtf}{rdentf} \qquad (2.4)$$

$$rnumtf = 2.094e04s^8 - 2.048e08s^7 + 3.378e11s^6 + 5.664e12s^5 + 8.5e18s^4$$
$$+ 2.093e21s^3 + 7.777e24s^2 + 4.899e26s + 1.159e30$$

$$rdentf = s^9 + 1345s^8 + 2.153e07s^7 + 2.339e10s^6 + 5.378e13s^5 + 4.01e16s^4$$
$$+ 3.574e19s^3 + 1.826e22s^2 + 5.025e24s + 2.091e27$$

The reduced system poles and zeros are given in the Table 2.1. All poles are in the left-half plane (LHP) or negative poles, which makes the plant a stable plant. There are five right-half plane (RHP) zeros and rest are LHP zeros. The RHP zeros are also known as non-minimum phase zeros and influences the the system behavior, controller design, and closed-loop bandwidth [16].

Table 2.1: Poles and Zeros of fine Y-stage model

Poles	Zeros
-160.04 + 4242.1i	1875.9 + 5450i
-160.04 - 4242.1i	1875.9 - 5450i
-42.583 + 3126.1i	3842.4 + 0i
-42.583 - 3126.1i	109.26 + 3247.3i
-19.071 + 1302i	109.26 - 3247.3i
-19.071 - 1302i	-596.75 + 2050.9i
-141.16 + 1206.6i	-596.75 - 2050.9i
-141.16 - 1206.6i	-22.246 + 1295.7i
-617.44 + 0i	-22.246 - 1295.7i
-8.1297 + 434.88i	-8.4026 + 437.62i
-8.1297 - 434.88i	-8.4026 - 437.62i

The RHP zeros causes a number of performance limitations. According to classical root-locus analysis, when the feedback gain is increased towards infinity then the closed-loop poles migrate towards the position of the open-loop zeros. So, even with a stable plant (all

15

poles in LHP), the closed-loop poles might migrate from LHP to the open-loop RHP zeros, making the closed-loop unstable.

According to [16], for a real RHP zero z the approximate requirement for bandwidth is,

$$\omega_b < z \qquad (2.5)$$

and the requirement for a complex-pair of RHP zeros z is,

$$\omega_b < \begin{cases} |z|/4 & : Re(z) \gg Im(z) \\ |z|/2.8 & : Re(z) = Im(z) \\ |z| & : Re(z) \ll Im(z) \end{cases}$$

In case of EUI, the real RHP zero for the fine Y-stage, $z3 = 3842.4 + 0i$ results in the upper-bound $\omega_b < (3842/2 = 1921)rad/s$ (305 Hz) for the closed-loop bandwidth. Similarly, for the complex pair of RHP zeros:

for $z1, z2 : \omega_b < |1875.9 + 5450i| = 5763rad/s$ (917 Hz)

for $z4, z5 : \omega_b < |109.26 + 3247.3i| = 3249.1rad/s$ (517 Hz)

That is the upper bound for closed-loop bandwidth due to the presence of RHP zeros is 305 Hz, but since that is greater than the open loop bandwidth (188 Hz) it does not create any limitations.

2.6   Model Verification
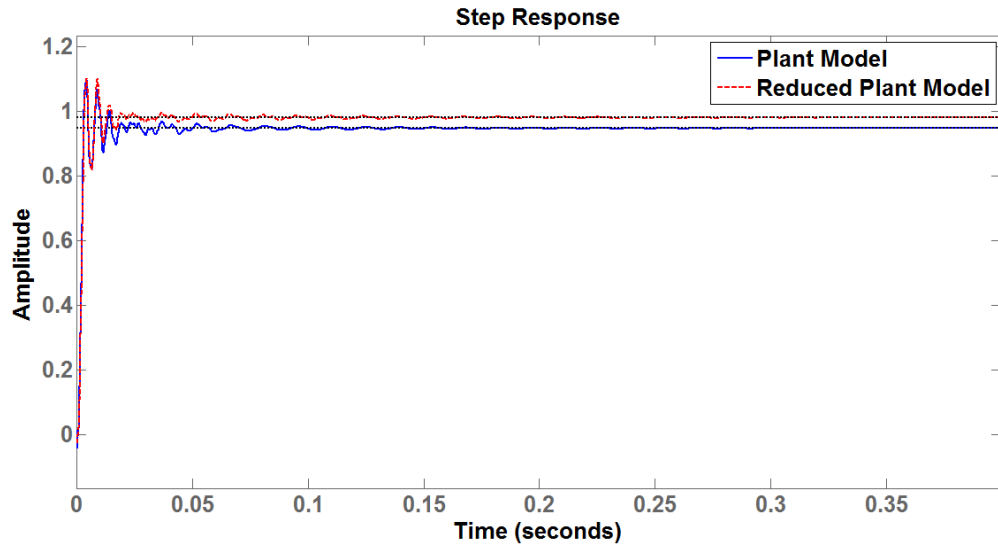
Figure 2.10: Open loop step response of fitted plant model and reduced plant model, both responses are converging close to 1.

The step response of the fitted model and reduced fitted model is shown in the Figure 2.10. the fine Y-stage sensitivity is 569.43 nm/V, which means for 1 volt input to the piezo-stack actuator the stage undergoes a displacement of 569.43 nanometers. As a qualitative measure of the fit tracking of a triangular wave of 75 nm amplitude and frequencies 20 Hz and 50 Hz are shown in the Figure 2.11 and Figure 2.12 respectively.
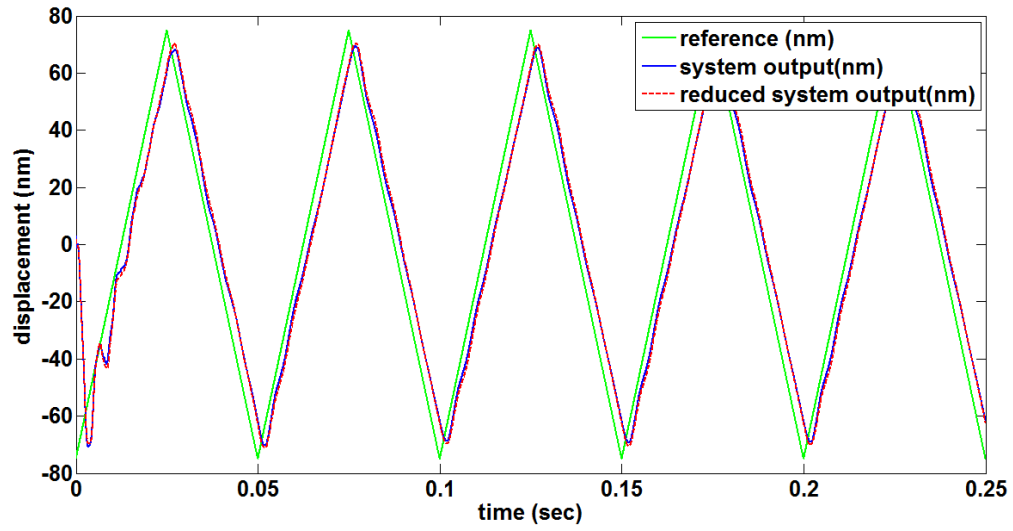
Figure 2.11: 20 Hz triangular wave tracking in open loop by the fitted plant model and reduced plant model.
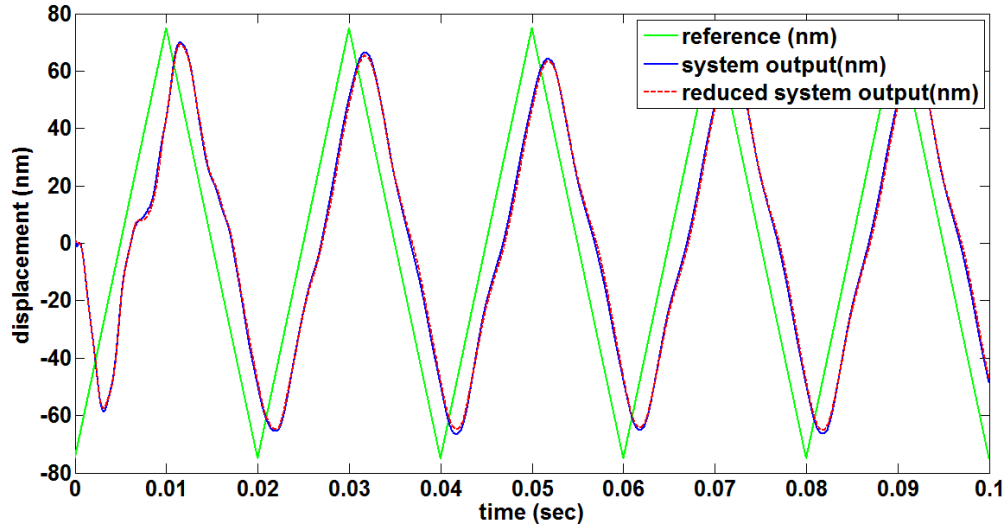
Figure 2.12: 50 Hz triangular wave tracking in open loop by the fitted plant model and reduced plant model.

18

2.7 Open Loop Resolution

To calculate the resolution of the open loop system a zero amplitude, zero frequency input was given to the system. That is the only signal going into the system was environmental noise and disturbance. The system output (Y-stage displacement) due to the environmental noise was measured. A histogram of the system output was then plotted shown in the Figure 2.13. It is clear that the noise histogram is skew symmetric. The reason behind this is that the open loop system output is slowly and continuously drifting away from the mean value. Also the noise-histogram of the open-loop system output has an offset mean and large standard deviation. The large standard deviation means that the data is widely dispersed or spread away from the average. Based on the standard deviation (σ), the $3\sigma-$ resolution of the open-loop data is approximately 7 nm ($3\sigma = 3 * 2.33$).
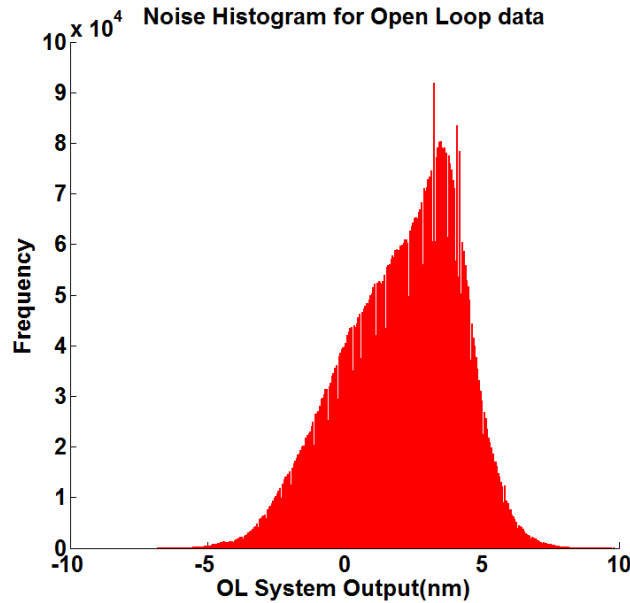
Figure 2.13: Noise histogram of open loop system output. The 3-σ resolution is approx 7 nm.

CHAPTER 3

CONTROLLER DESIGN AND IMPLEMENTATION

Previously PID controllers with low bandwidth were designed and implemented on EUI. A group of WINDOWS-2000 industrial PC and standard National Instruments LabVIEW were used to implement the controllers. Although the exact bandwidth of the implemented PID controllers are unknown, the bandwidth limitation stemmed from the aspects such as the underlying operating system on which LabVIEW was running was WINDOWS-2000 which is not a true real time system and the signal communications were made using slow RS-232 connection.

The work in this thesis is focused on design and implementation of high-end controllers giving robust stability, high bandwidth, high resolution, disturbance rejection and noise attenuation. First, a PID controller was designed and implemented due to its ease of design and simplicity in implementation. The PID controllers also served as a good baseline to which the other controllers would be compared. Comparison with originally implemented controllers was not possible since the previous controller hardware is no longer working. Also this was an important step in implementing the controllers for the first time using the National Instruments (NI) CompactRIO hardware. The discrete controllers were represented by biquad structures directly in the FPGA fabric. Verification of implementation of PID controllers were done by checking the simulation and experimental closed-loop transfer functions, plant model and tracking etc.

Figure 3.1: National Instruments CompactRIO hardware with real-time controller and FPGA on chassis.(Courtesy NI website)

All the implementation issues were addressed during the implementation of PID controllers. Ground for arbitrary controller implementation was then set. The next controller designed was a H_∞ controller well known as the Glover-McFarlane controller. Glover-McFarlane controller robustly stabilizes an already existing PID or any other industrial controller in closed-loop. To achieve robust stability through Glover-McFarlane controller design some bandwidth is sacrificed. Up to an eighth order Glover-McFarlane controller was implemented using the biquad structure and utilizing the CompactRIO hardware. Although the Glover-McFarlane controller design provides robust stability it is not a truly flexible H_∞ controller design. A truly flexible design algorithm is the one that ensures robust stability, bandwidth and resolution requirements and provides the flexibility to choose and optimize the target criterion. 1 DOF H_∞ controllers up to 16th order were successfully implemented. Also larger bandwidth and resolution was achieved.

3.1 PID Controller Algorithm

The advantage of a PID control algorithm is that it is applicable to most control systems. The usual version of PID controller is given by the following equation,

$$u(t) = K \left(e(t) + \frac{1}{T_i} \int_0^t e(\tau)\, \mathrm{d}\tau + T_d\, \frac{\mathrm{d}e(t)}{\mathrm{d}t} \right) \tag{3.1}$$

Where, $u =$ the control signal, $e = r - y =$ the control error, $r =$ reference signal. The control signal is made up of the sum of the proportional term, integral term, and the derivative term. The proportional term is proportional to the control error, the integral term is proportional to the integral of the control error, and the derivative term is proportional to the derivative of the control error. The integral term makes the steady-state error go to zero. And the derivative term gives a prediction of future error and thus improves closed-loop stability. PID controller has following three controller parameters:
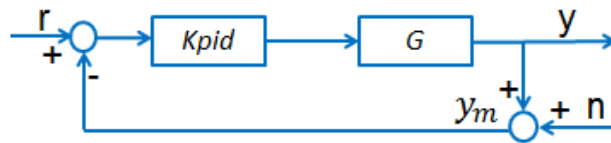$K =$ proportional gain, $T_i =$ integral time, and $T_d =$ derivative time.

Figure 3.2: A schematic showing the PID controller.

Figure 3.2 shows a PID controller in feedback loop with the identified transfer function

model G_y of fine Y-stage. Where, r = reference signal, y = system output or Y-stage vertical position, n = measurement noise, y_m = measured system output. The loop is in negative feedback format.

The PID controller algorithm represented in the transfer function form:

$$U(s) = K \left(1 + \frac{1}{sT_i} + sT_d \right) \tag{3.2}$$

$$U(s) = K_P + \frac{K_I}{s} + K_D\, s \tag{3.3}$$

Equation 3.2 is known as the standard or non-interacting form of the PID algorithm. Whereas, equation 3.3 is known as the parallel form of PID control algorithm. Where, $K_P = K$, $K_I = \frac{K}{T_i}$, and $K_D = K\, T_d$.

The motivation for working on a PID controller is that it is simple to design and implement. The PID controllers designed for EUI usually are only a first order controller. This makes it very easy to implement and requires very little resources during FPGA implementation.

3.1.1   Design

The PID controller was designed using the MATLAB Simulink PID controller block. The controller form chosen was the parallel form, where the output is the sum of the proportional, integral, and derivative actions weighted by the gain parameters K_p, K_I, and K_D.

$$K_{PID} = K_P + K_I \frac{1}{s} + K_D \frac{N\, s}{(N\, +\, s)}; \tag{3.4}$$

Where, N is the filter coefficient, which sets the location of the pole in the derivative filter. PID controllers were designed by tuning the design parameters K_p, K_I,, K_D and N. The objective was to design stable PID controllers with as high bandwidth as possible. First, the PID controller gains were automatically tuned to produce a stable PID controller with nominal performance and low bandwidth. At this point no other design parameters like bandwidth requirement or time domain properties were mentioned, except the default values already in place to start with. Next the controller parameters and gains were varied manually to design PID controllers with higher bandwidth in both time-domain and frequency-domain design mode.

Second phase, of the design is to verify the performance of the designed discrete controllers in Simulink simulation and LabVIEW simulation. The designed continuous-time controllers were discretized using Tustin's method. The sampling time of discretization was $40\, \mu\, sec$.
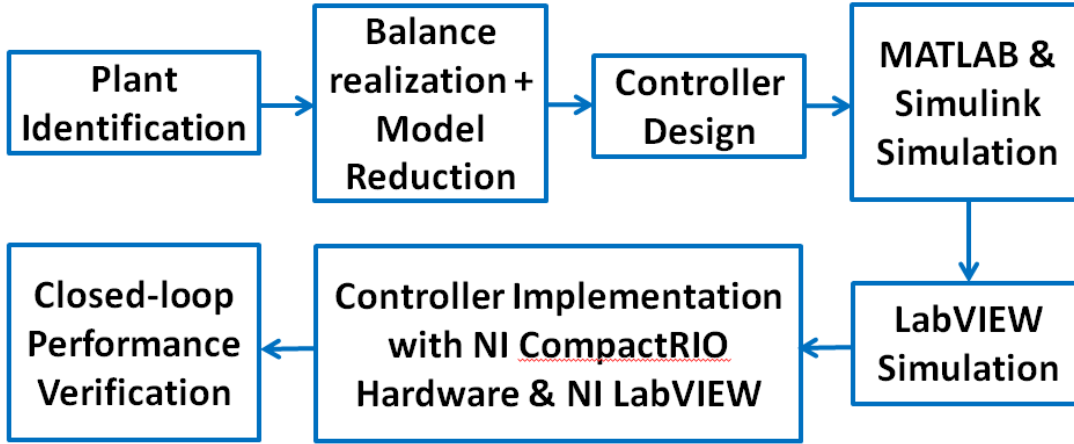
22

Figure 3.3: A block diagram showing the step-by-step process of desigining and implementing a controller.

In other words, the controllers are designed to run at a rate of 25 kHz. MATLAB function *c2d* was used to convert the continuous time transfer function to discrete time transfer function. In the Simulink simulation model the controller were represented in biquad structure (detailed in the implementation part) and the plant was a continuous time transfer function model. In LabVIEW simulation both the controller and the identified plant model were represented by biquad structures. The independent simulations in Simulink and LabVIEW verified the performance of the designed discrete time control algorithms.

3.1.2 Implementation

The controller was implemented utilizing the NI CompactRIO hardware and NI LabVIEW software. NI CompactRIO system includes I/O modules, a reconfigurable FPGA chassis, and an embedded real-time controller. The discrete controllers are run at a certain rate (here 25 kHz, flexibly specifiable) on the FPGA that is in the CompactRIO chassis. The existing function blocks for PID controller and transfer function in the LabVIEW FPGA library has some limitations. Controller transfer functions having an order more than two were not successfully implementable using the existing transfer function block. So, an alternative way of representing the transfer functions in the FPGA needed to be found. The biquad structure [17] or the "second order sections" shown in Figure 3.4 was utilized, which is basically a discrete filter. One biquad or one second order section represents a second order transfer functions. Using the second order sections in series, any order controller transfer function can be represented. In both LabVIEW simulations on FPGA and LabVIEW experiment implementation on EUI system through FPGA the controllers were represented by biquads.

23
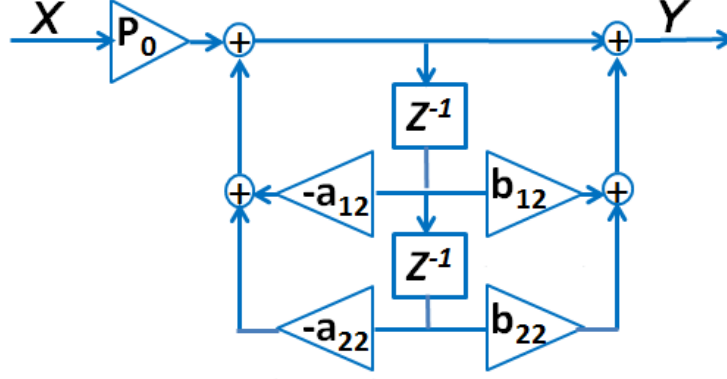
Figure 3.4: A Biquad structure showing one second order section that can represent a second order transfer function.

A stable PID controller up to bandwidth of 38 Hz were implemented successfully on the EUI fine Y-stage. The bode plot of the PID controller is shown in Figure 3.5. The transfer function of the PID controller is as follows:

$$K_{PID} = \frac{6.237e - 05\, s^2 + 0.7285\, s + 209}{s^2 + 350\, s} \qquad (3.5)$$
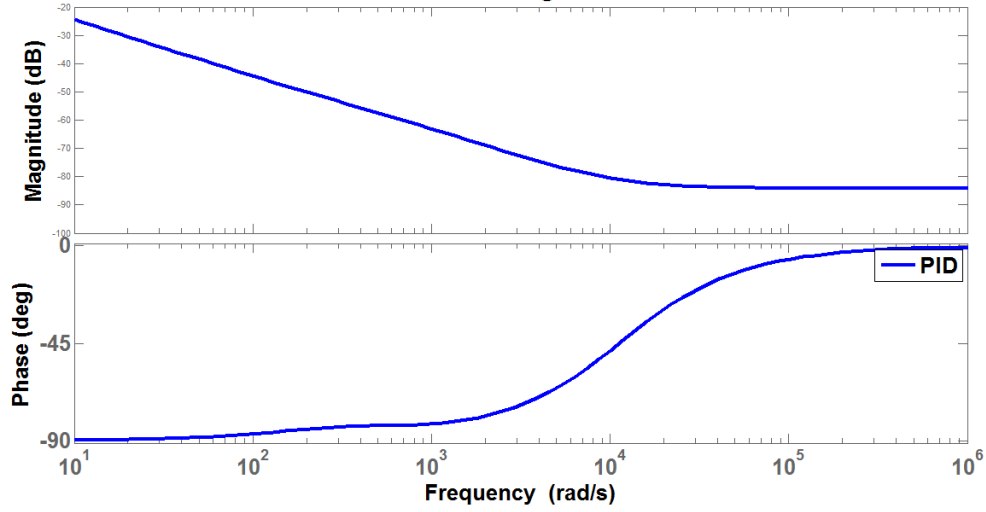
Figure 3.5: Bode plot of a 38 Hz bandwidth PID controller.

$$e = r - y = r - G_y u = r - G_y K e \qquad (3.6)$$

$$e = (1 + G_y K)^{-1} r = S r \qquad (3.7)$$

$$y = G_y u = G_y K e = G_y K (r - y) \qquad (3.8)$$

$$y = (1 + G_y K)^{-1} G_y K r \qquad (3.9)$$

$$S = 1/(1 + G_y K) \qquad (3.10)$$

$$T = G_y K/(1 + G_y K) \qquad (3.11)$$

Where, S is the sensitivity transfer function, which is a closed-loop transfer function from reference r to error signal, $e = r - y$, and T, known as the complementary sensitivity transfer function, is the closed-loop transfer function from reference r to the system output y. The sensitivity transfer function can also be expressed as $\frac{dy/y}{dG_y/G_y}$ that represents the percentage change in the plant output to percentage change in the plant model. In other words, S gives a measure of robustness of the closed-loop system to uncertainty in the identified plant model G_y. A general criteria for robust stability of the closed-loop the peak of the sensitivity transfer function, S should be less than 5 - 6 dB or, in other words,

$$\|S\|_\infty \leqslant 2 \qquad (3.12)$$

The bandwidth ω_b is determined based on the frequency corresponding the point of crossing of the -3 dB line by the sensitivity transfer function. For larger bandwidth it is needed that S crosses the -3 dB line as later as possible. Similarly, ω_{bt} is the bandwidth based on the complementary sensitivity transfer function T by its the crossing of the -3 dB line from above. Smaller the value of ω_{bt} the greater the resolution. Bandwidth ω_{bt} would be smaller if T has higher roll-off rate, which in turn mean higher resolution. Since, $y = Tr$ so it is expected that the value of T be approximately be equal to 1 in the frequency region good tracking is required. These, requirements would also determine the shape of T transfer function.

To verify if the closed-loop is working as expected, identification of plant transfer function, sensitivity transfer function (S), and complementary sensitivity transfer function (T) were performed. From Figure 3.6 it is clear that the experimental closed-loop plant model and open loop plant model are closely matched. The resonance peaks show that both plants have resonant peak at same frequency. And also the DC value of both plants are also the same. The low frequency and the high frequency peaks are captured and also match.

The bode plot of closed-loop sensitivity transfer function (S) and complementary sensitivity transfer function (T) for simulation and experiment are plotted in the Figure 3.7 and
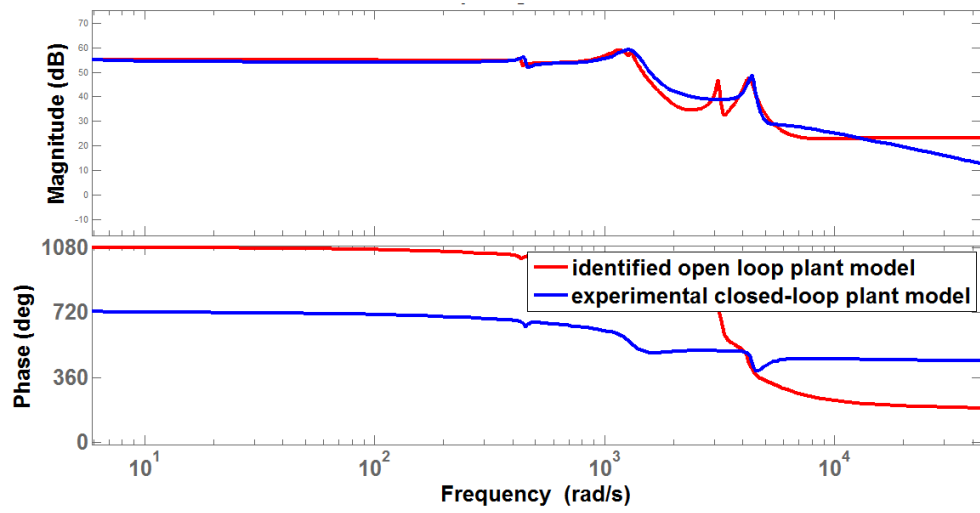
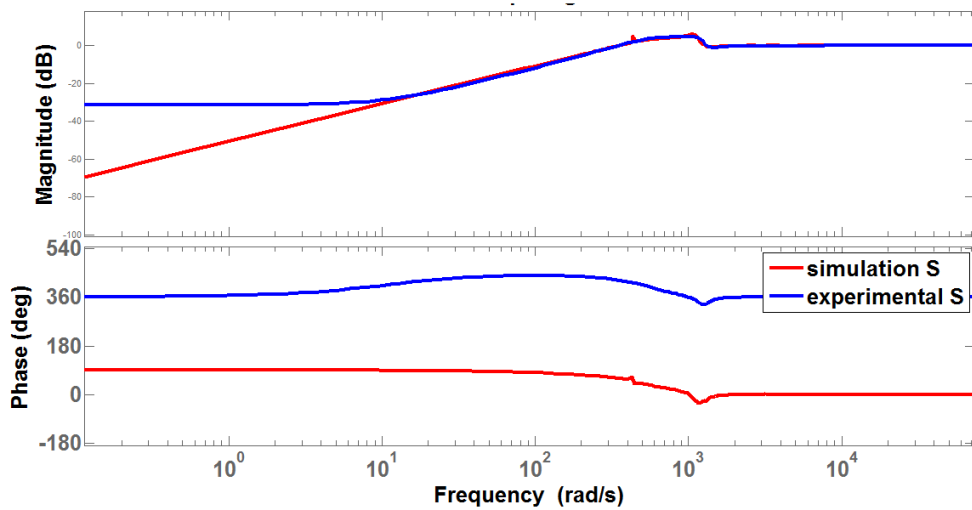Figure 3.6: Bode plot of open loop identified plant model and closed-loop identified plant model.

Figure 3.7: Bode plot of Sensitivity transfer function, S in simulation and experiment. Sensitivity peak is approximately 4.768 dB, which is below 5 - 6 dB line.

Figure 3.8 respectively. The S and T transfer functions do match well. The bandwidth based on the crossing of -3 dB line of S transfer function from below, gives $\omega_{b\,sim} = 38Hz$ and $\omega_{b\,exp} = 40Hz$ for simulation and experimental respectively. The bandwidth based on T transfer function are $\omega_{bt\,sim} = 189Hz$ and $\omega_{bt\,exp} = 192Hz$ for simulation and experimental respectively.
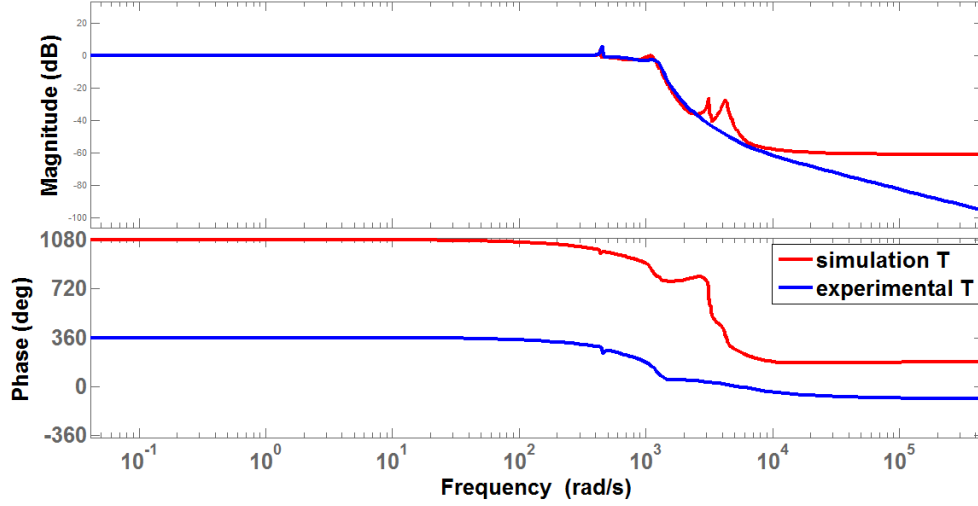
Figure 3.8: Bode plot of Complementary Sensitivity transfer function, T in simulation and experiment.

The closed-loop transfer function KS needs to be bounded so that the controller output u is bounded. Since, in most of the cases there is hardware bound of the maximum magnitude input that the system can handle, bounding controller output to avoid controller saturation is important. The closed-loop transfer function GS needs to be small in the frequency region of interest for good disturbance rejection, since GS is the transfer function from a disturbance, d (at the plant input) to the plant output y. The bode plot of KS and GS transfer functions for simulation and experiment are plotted in the Figure 3.9 and Figure 3.10 respectively. The simulation and experimental KS transfer functions match pretty well. The magnitude of the KS transfer function is clearly staying bounded over all frequencies. Note the hardware limit of plant input for the EUI is -5 V to 5 V. At low frequencies the GS transfer function matches the shape of S and at high frequencies it matches that of the plant transfer functions.

Tracking of triangle wave with 75 nm amplitude and frequencies 20 Hz and 100 Hz by the 38 Hz bandwidth PID controller is shown in the Figure 3.11. Clearly, the PID controller tracks 20 Hz triangular wave better than the 100 Hz one. Also there is larger offset of the output signal for the tracking of the 100 Hz triangular wave.

To calculate the resolution of the closed loop system zero amplitude, and zero frequency input was given to the system and the system output was measured. A noise histogram of
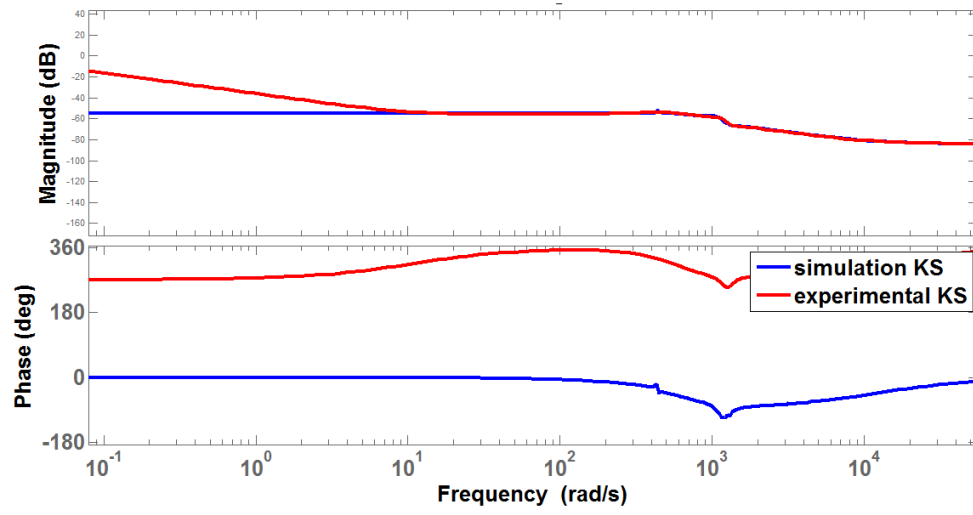
Figure 3.9: Bode plot of KS function in simulation and experiment.
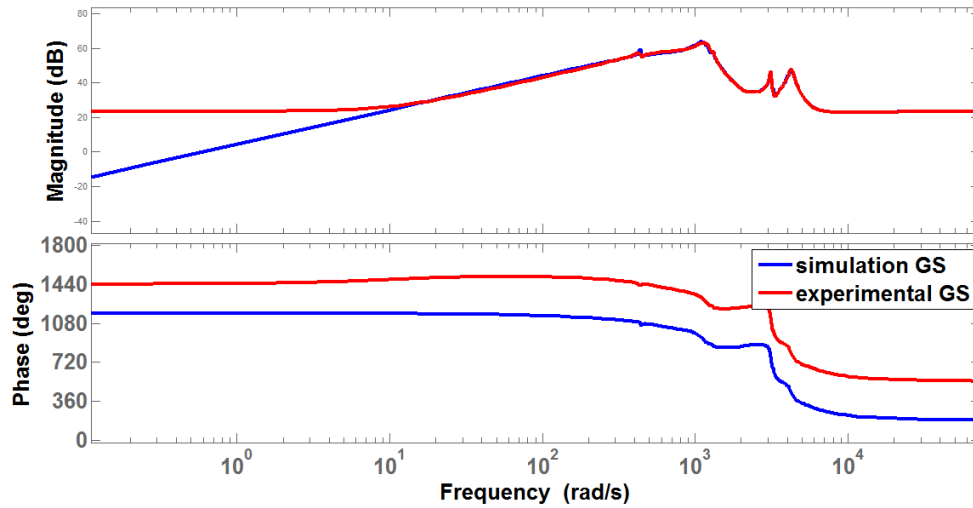
Figure 3.10: Bode plot of GS function in simulation and experiment.

(a) 20 Hz Triangle Tracking   (b) 100 Hz Triangle Tracking
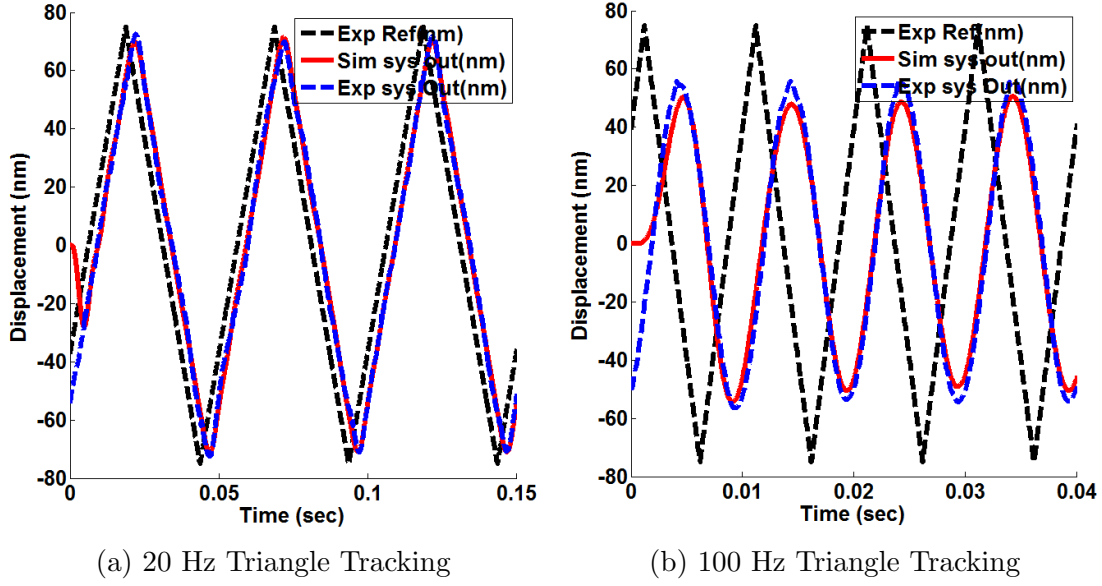
Figure 3.11: Triangular wave tracking verification of 38 Hz bandwidth PID controller

the closed-loop system output and open loop system output is shown in the Figure 3.12. The noise histogram for closed-loop is symmetric and has smaller standard deviation than open loop. Based on the standard deviation $(\sigma), the\ 3\sigma-$ resolution of the closed-loop data is approximately 3.9 nm ($3\sigma = 3 * 1.3$). That is 143% improvement of resolution over open loop system.
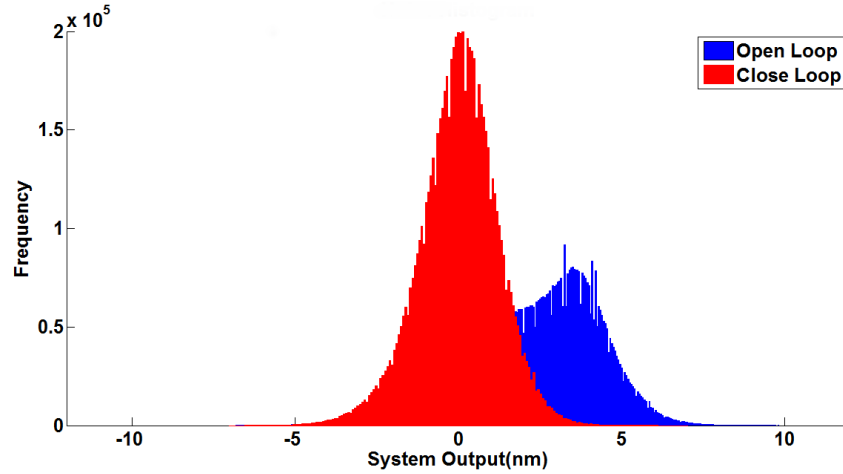
Figure 3.12: Closed-loop noise histogram with a 38 Hz PID controller giving a resolution of approx 3.9 nm. Whereas the open loop resolution is approx 7 nm.

3.2 Glover-McFarlane Controller Algorithm

Glover-McFarlane controller [12] algorithm is a H_∞ − robust stabilization algorithm formulated by Keith Glover and Duncan McFarlane. This algorithm considers the stabilization of a system, for purpose of this thesis the fine Y-stage system G_y, taking the fact that G_y has a normalized left coprime factorization, given by

$$G_y = M^{-1} N \tag{3.13}$$

Where, $M \, \& \, N$ are normalized such that they satisfy the following Bezout identity:

$$M \, M^* + N \, N^* = I \tag{3.14}$$
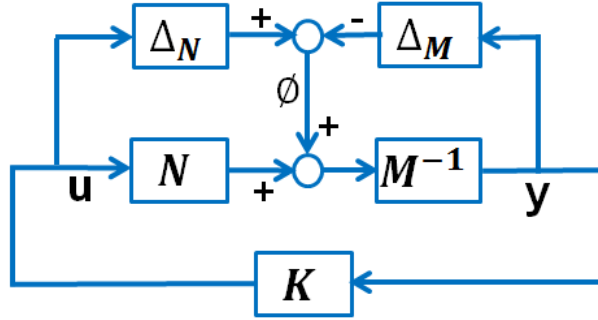
Figure 3.13: Robust stabilization of a family of perturbed plants [12, 16].

Given this definition of plant factorization a perturbed plant can be formulated as,

$$G_{py} = (M + \Delta_M)^{-1} \, (N + \Delta_N) \tag{3.15}$$

Where, Δ_M, Δ_N are plant uncertainty in the nominal plant G_y, both being stable transfer functions. A family of such perturbed plants can be represented as:

$$G_{py} = \left\{ (M + \Delta_M)^{-1} \, (N + \Delta_N) : || \, [\Delta_N \ \ \Delta_M] \, ||_\infty < \epsilon \right\} \tag{3.16}$$

Glover-McFarlane controller algorithm objective is to obtain closed-loop stability for all plants in the family of perturbed plants for a stability margin, $\epsilon > 0$. This algorithm tries to maximize the stability margin to get, ϵ_{max}. The maximum robust stability margin is

$$\epsilon_{max} = \left\{ 1 - ||[N \ \ M]||_H^2 \right\}^{-\frac{1}{2}} = (1 + \rho \, (X \, Z))^{\frac{1}{2}} \tag{3.17}$$

Now, for robust stability of the closed-loop, the following two criterions need to be fulfilled:

1. The nominal close loop needs to be stable

2.

$$\gamma = ||\begin{bmatrix} K \\ I \end{bmatrix} (I - G_y K)^{-1} M^{-1} ||_\infty \ \leq \ \frac{1}{\epsilon} \tag{3.18}$$

Where, $||\,.\,||_H$ is the so called Hankel norm, ρ is the spectral radius i.e. maximum eigenvalue. X and Z are unique positive definite solutions of following two algebraic Riccati equations respectively.

$$(A - BS^{-1}D^T C)\,Z \ + \ Z(A - BS^{-1}D^T C)^T \ - \ ZC^T R^{-1}CZ \ + \ BS^{-1}B^T \ = \ 0 \tag{3.19}$$

$$(A - BS^{-1}D^T C)^T\,X \ + \ X(A - BS^{-1}D^T C) \ - \ XBS^{-1}B^T X \ + \ C^T R^{-1}C \ = \ 0 \tag{3.20}$$

$$R \ = \ I \ + \ DD^T, \ \ S \ = \ I \ + \ D^T D \tag{3.21}$$

$$\gamma_{min} \ = \ \frac{1}{\epsilon_{max}} \tag{3.22}$$

Designing an optimal controller can be very hard and computationally heavy. In practice designing an optimal controller is not necessary. Since, a controller resulting from a sub-optimal γ slightly greater than the optimal γ_{min} is closely matched from performance perspective. There is no substantial gain to achieve from designing an optimal controller. So, a suboptimal $\gamma > \gamma_{min}$ is chosen to achieve the following suboptimal Glover-McFarlane controller.

$$K \ = \ \left[\begin{array}{c|c} A \ + \ BF \ + \ \gamma^2 (L^T)^{-1} ZC^T (C \ + \ DF) & \gamma^2 (L^T)^{-1} ZC^T \\ \hline B^T X & -D^T \end{array} \right] \tag{3.23}$$

$$F \ = \ -S^{-1}(D^T C \ + \ B^T X) \tag{3.24}$$

$$L \ = \ (1 - \gamma^2)\,I \ + \ XZ \tag{3.25}$$

3.2.1 Design

As seen in the Figure 3.14, the PID controller K_{PID} and the plant G_y makes up the shaped plant G_s. Controller K_s is designed on the shaped plant G_s to make the closed loop robustly stable. The main advantage of a Glover-McFarlane controller is that it can be used on an existing industrial controller or a PID controller, K_{PID} to introduce robust stability in the closed-loop at the price of little bandwidth. The maximum stability margin was calculated by the equation 3.17 to give 0.54. And from it optimal $\gamma_{min} = 1.8473$ is calculated. A sub-optimal $\gamma = 1.8482$ is chosen, to design a sub-optimal Glover-McFarlane controller with 38 Hz bandwidth.
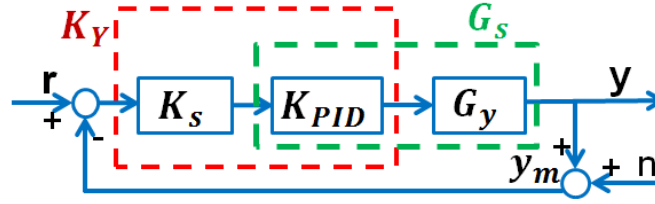
Figure 3.14: A schematic showing the Glover-McFarlane controller.

3.2.2 Implementation

Glover-McFarlane controllers were also discretized using the Tustin's method and then the coefficients of the biquad structure of the controller were used to implement on EUI fine Y-stage. Controllers up to bandwidth (based on S) of 38 Hz were implemented. In particular the 9th order 38 Hz bandwidth robustly stable Glover-McFarlane controller was designed based upon an unstable 62 Hz bandwidth PID controller. The bode plot of the 38 Hz controller is given in Figure 3.15. The transfer function of the GM controller is given as follows:

$$K_{GM} = \frac{numtf}{dentf} \tag{3.26}$$

$$
\begin{aligned}
numtf &= -1.584e - 06s^9 + 166.8s^8 + 8.255e05s^7 + 2.5e09s^6 + 9.564e12s^5 + 8.713e15s^4 \\
&\quad + 1.37e19s^3 + 6.821e21s^2 + 2.334e24s + 9.673e26 \\
dentf &= s^9 + 3.309e05s^8 + 7.617e08s^7 + 4.477e12s^6 + 8.618e15s^5 + 1.173e19s^4 + 1.187e22s^3 \\
&\quad + 2.226e24s^2 + 1.946e27s + 1.583e14
\end{aligned}
$$

To verify the closed-loop transfer functions, identification of plant transfer function, sen-

Figure 3.15: Bode plot of the 38 Hz bandwidth Glover-McFarlane controller.

sitivity transfer function (S), and complementary sensitivity transfer function (T) was performed. The experimental closed-loop plant model and open loop plant model are closely matched as seen in Figure 3.16. The resonance peaks show that both plants have resonant peak at same frequency. And also the DC value of both pl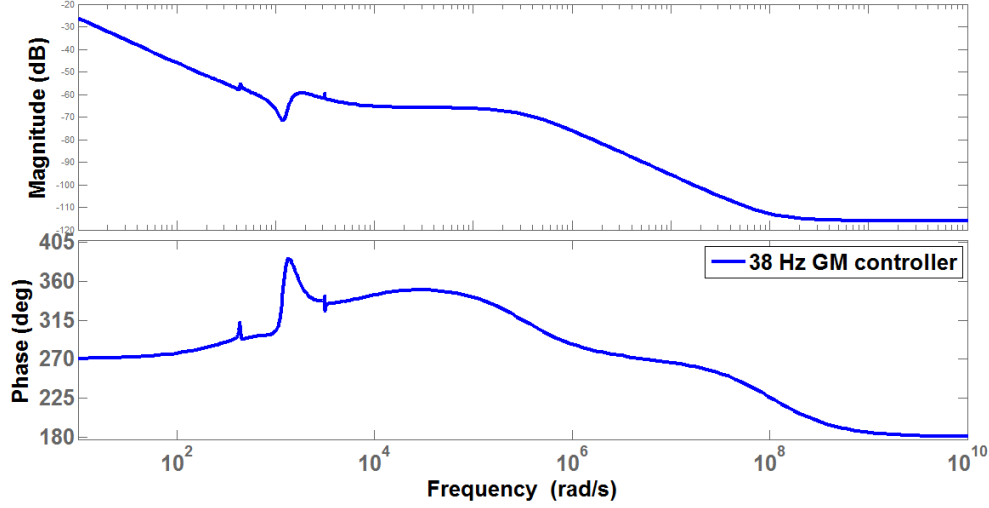ants are also the same. Note that the open loop plant was identified from average of 10 different datas, whereas the closed-loop one was obtained from one data. The missing peak in the closed-loop plant was present in the non-parametric transfer function estimate done by *tfestimate*, but was not fitted by the curve fitting process. The bode plot of closed-loop sensitivity transfer function (S) and complementary sensitivity transfer function (T) for simulation and experiment are plotted in the Figure 3.17 and Figure 3.18 respectively. The S and T transfer functions do match well. The bandwidth based on the S transfer function, gives $\omega_{b\,sim} = 38Hz$ and $\omega_{b\,exp} = 37Hz$ for simulation and experimental respectively. The bandwidth based on T transfer function are $\omega_{bt\,sim} = 74Hz$ and $\omega_{bt\,exp} = 83Hz$ for simulation and experimental respectively. Sensitivity transfer function peak in the bode plot is approximately 4.76 dB, which assures robust stability since peak of the S transfer function is below 5 - 6 dB line (Robust Stability criterion).

The bode plot of KS and GS transfer functions for simulation and experiment are plotted in the Figure 3.19 and Figure 3.20 respectively. The simulation and experimental transfer functions match pretty well.The magnitude of the KS transfer function is clearly staying bounded over all frequencies. At low frequencies the GS transfer function matches the shape of S and at high frequencies it matches that of the plant transfer functions.

Tracking of triangle wave with 75 nm amplitude and frequencies 20 Hz and 100 Hz by the 38 Hz bandwidth Glover-McFarlane controller is shown in the Figure 3.21. As expected,
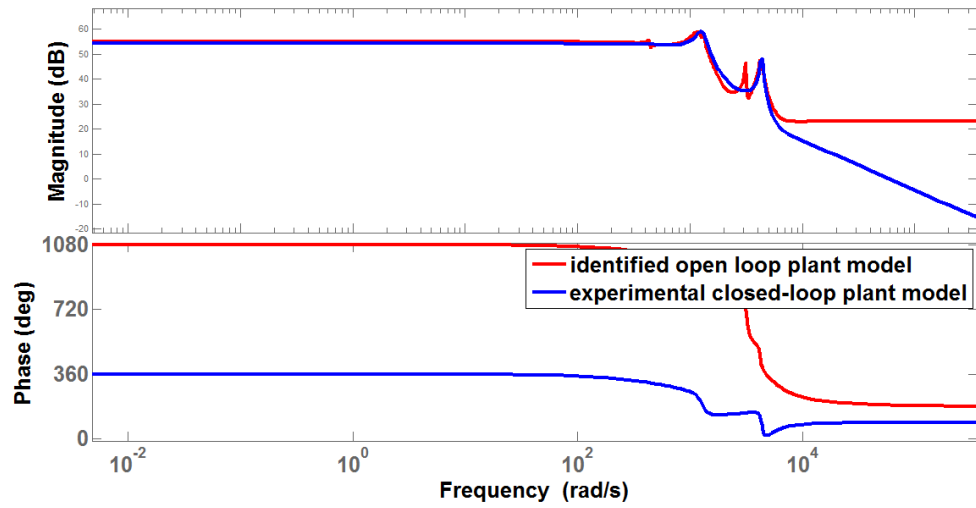
Figure 3.16: Bode plot of the open loop identified plant model and the closed-loop identified plant model.
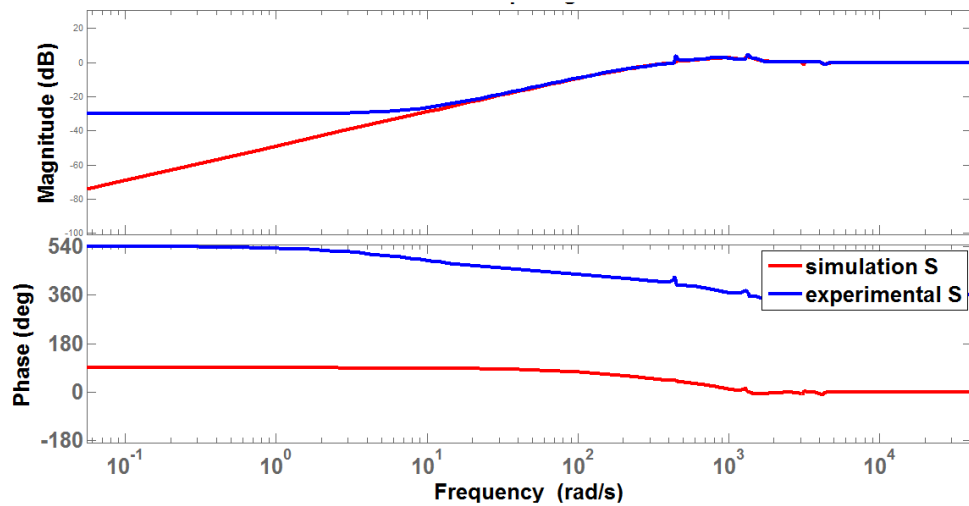
Figure 3.17: Bode plot of Sensitivity transfer function, S in simulation and experiment. Sensitivity peak is approximately 4.76 dB, which is below 5 - 6 dB line.
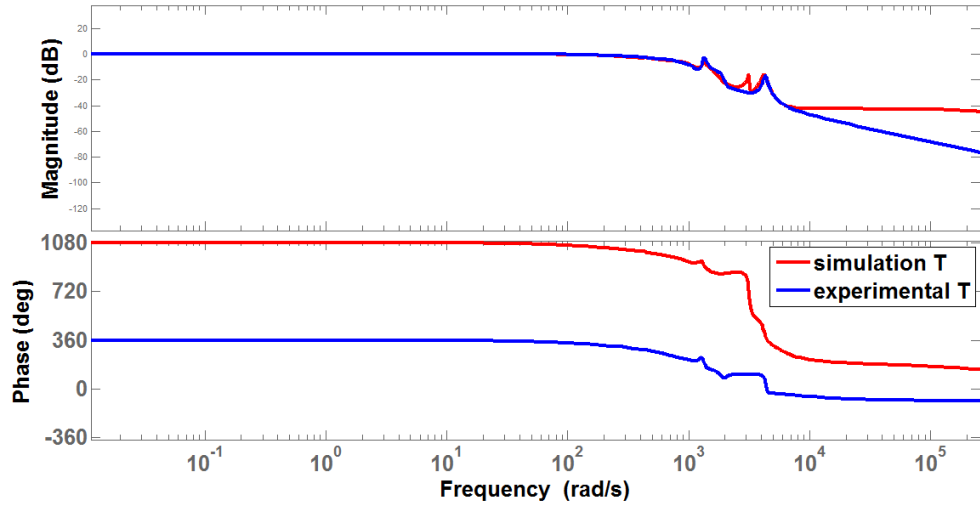
Figure 3.18: Bode plot of Complementary Sensitivity transfer function, T in simulation and experiment.
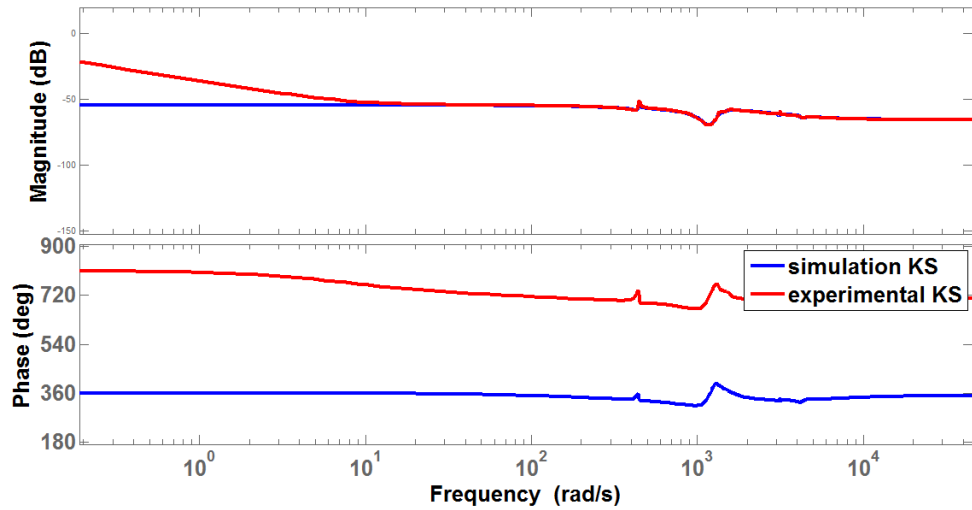
Figure 3.19: Bode plot of KS function in simulation and experiment.
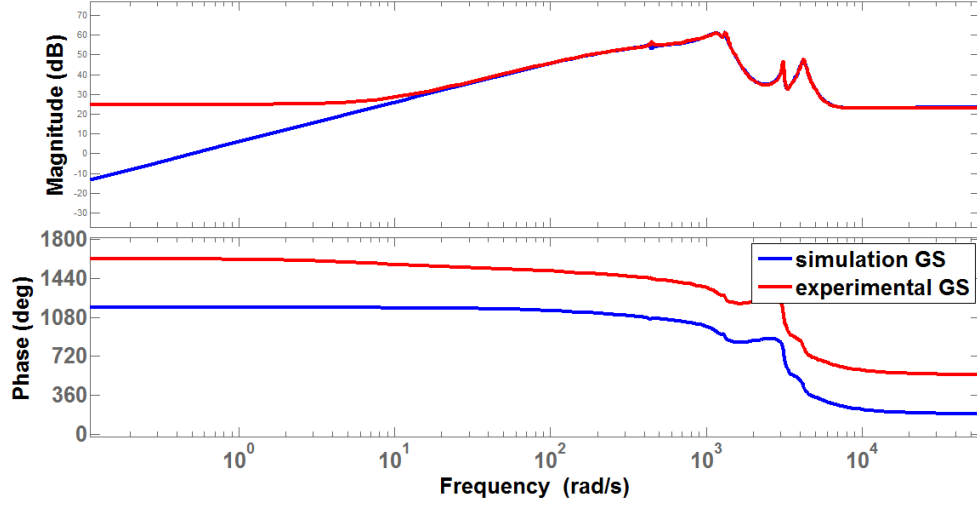
Figure 3.20: Bode plot of GS function in simulation and experiment.

the GM controller tracks 20 Hz triangular wave better than the 100 Hz triangular wave. Since, the PID controller and the Glover-McFarlane controller has equal bandwidth (38 Hz) there is no noticeable improvement of tracking. Note that this Glover-McFarlane controller (although with 38 Hz banwidth) is robustly stable, compared to the unstable 62 Hz PID controller it is based upon.

(a) 20 Hz Triangle Tracking

(b) 100 Hz Triangle Tracking
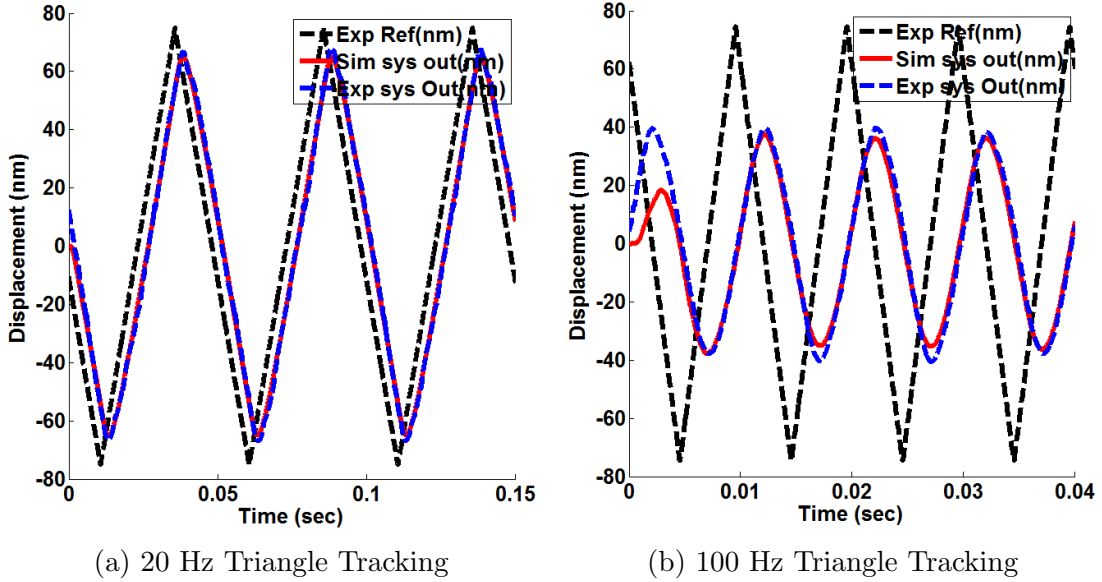
Figure 3.21: Triangular wave tracking by 38 Hz bandwidth Glover-McFarlane controller.

To calculate the resolution of the closed-loop system with Glover-McFarlane controller zero amplitude, and zero frequency input was given to the system and the system output was measured. A noise histogram of the closed-loop system output and open loop system

36
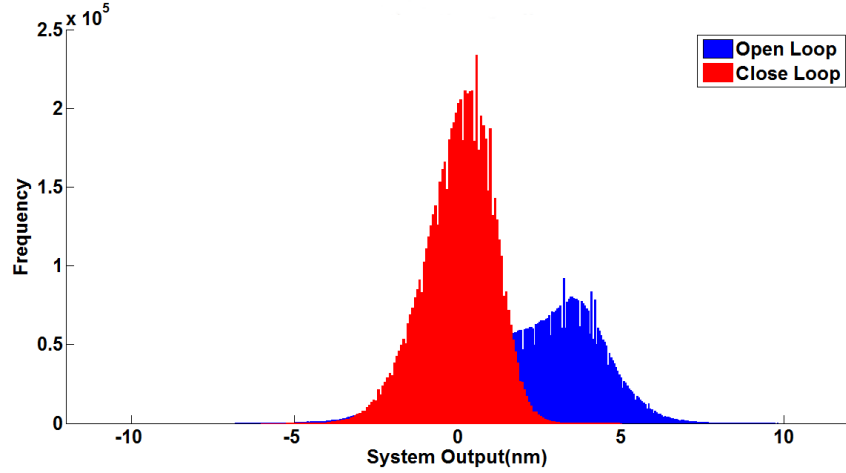
Figure 3.22: Closed-loop noise histogram with a 38 Hz Glover-McFarlane controller giving a resolution of approx 3.1 nm. Whereas the open loop resolution is approx 7 nm.

output is shown in the Figure 3.22. The noise histogram for closed-loop is symmetric and has smaller standard deviation than open loop. Based on the standard deviation $(\sigma), the$ $3\sigma-$ resolution of the closed-loop data is approximately 3.1 nm ($3\sigma = 3*1.03$). That is 155% improvement of resolution over open loop system. And a 120% improvement of resolution over PID controller.

3.3 H_∞ Controller Algorithm

The main advantage of the Glover-McFarlane controller algorithm presented in the previous section is that it provided robust stability to the closed-loop with an already existing controller. Other than the improvement in robust stability property, there was no significant improvement over PID controllers from the point of bandwidth and resolution. In addition, the algorithm is not flexible enough to incorporate parameters and quantifiable trade-offs required to better address the closed-loop properties. A more flexible controller algorithm is the 1 DOF H_∞ controller design that gives the flexibility of quantifying trade-offs between performance objectives, and calculates the feasibility of the desired specifications. The closed-loop transfer functions, that define the bounds for bandwidth, resolution, disturbance rejection, noise attenuation, and gives better tracking or regulation, can be shaped properly. The H_∞ algorithm gives a generalized framework through which the desired closed-loop objectives can addressed.

(a) S/T/KS mixed-sensitivity optimization, standard form for tracking

(b) General control configuration
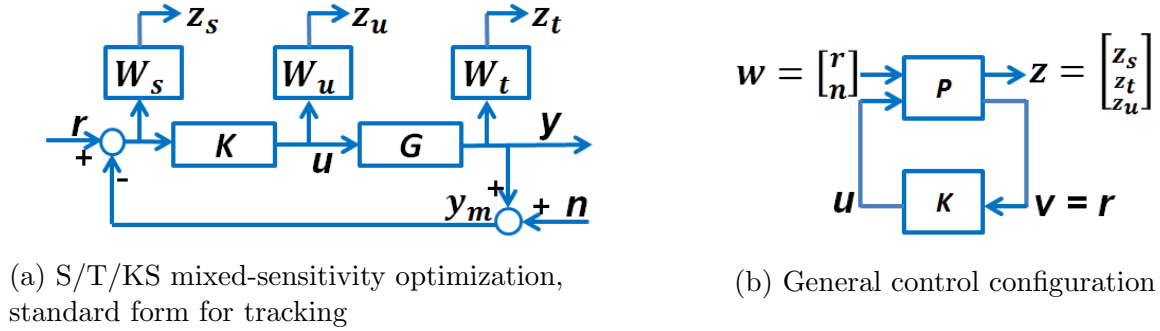
Figure 3.23: 1 DOF H_∞ controller design.

The controller K that is to be designed for the fine Y-stage (of the optics stage group) system G_y is in negative feedback orientation, as shown in Figure 3.23a. r is the reference that the system needs to track in closed-loop and n being the noise in the surroundings that comes in as a part of the measured system output, y_m.

Where $y_m = y + n$

Sensitivity transfer function, $S = (1 + GK)^{-1}$

Complementary sensitivity transfer function, $T = GK (1 + GK)^{-1} = I - S$

The closed-loop objectives are as follows:

- The controller K needs to stabilize the system G_y.

- For disturbance rejection the maximum singular value of S needs to be small

- For reference tracking the maximum singular value of $T \approx 1$

- For noise attenuation the maximum singular value of T needs to be small

- For control energy to be small the maximum singular value of KS needs to be small

In the 1 DOF H_∞ algorithm the closed-loop transfer functions S, T, and KS are shaped to satisfy the above mentioned closed-loop objectives. The shaping of the closed-loop transfer functions are done by designing weights W_s, W_t, and W_u on S, T, and KS respectively. The weights are designed in such way so that the H_∞ algorithm minimizes the H_∞ norm of the weighted closed-loop transfer functions $\|W_p S\|_\infty$, $\|W_t T\|_\infty$, and $\|W_u KS\|_\infty$ for some stabilizing controller K. i.e. Since, other closed-loop transfer functions are shaped in addition to the sensitivity transfer function, S, this is also known as the mixed sensitivity minimization H_∞ control algorithm.

This mixed-sensitivity problem as expressed in Figure 3.23a can be expressed in the general control configuration shown in Figure 3.23b. Here, $w = r$ is the exogenous input signals, u are the control signals, v are the measured variables, and $z = [z_s \; z_t \; z_u]$ are the error signals. P is the generalized plant which contains the nominal plant G_y and all the weights W_s, W_t, and W_u. The controller K is the robustly stabilizing H_∞ controller that provides with all the closed-loop objectives.

$$
\begin{bmatrix}
z_s \\
z_t \\
z_u \\
\hline
v
\end{bmatrix}
=
\left[
\begin{array}{c|c}
\begin{matrix} W_s \\ 0 \\ 0 \end{matrix} & \begin{matrix} -W_s G_y \\ W_t G_y \\ W_u \end{matrix} \\
\hline
I & -G_y
\end{array}
\right]
\begin{bmatrix}
r \\
\hline
u
\end{bmatrix}
\tag{3.27}
$$

$$
\begin{bmatrix}
z \\
\hline
v
\end{bmatrix}
=
\left[
\begin{array}{c|c}
P_{11}(s) & P_{12}(s) \\
\hline
P_{21}(s) & P_{22}(s)
\end{array}
\right]
\begin{bmatrix}
w \\
\hline
u
\end{bmatrix}
= P(s)
\begin{bmatrix}
w \\
\hline
u
\end{bmatrix}
\tag{3.28}
$$

Lets consider, that the generalized plant has the following state-space realization,

$$
P(s) =
\left[
\begin{array}{c|cc}
A & B_1 & B_2 \\
\hline
C_1 & D_{11} & D_{12} \\
C_2 & D_{21} & D_{22}
\end{array}
\right]
\tag{3.29}
$$

The H_∞ norm of the close-loop transfer function from w to z is minimized in the H_∞ controller design process. This closed-loop transfer function is given by the lower linear fractional transformation, given as follows,

$$
F_l(P, K) = P_{11} + P_{12} K (I - P_{22} K)^{-1} P_{21}
\tag{3.30}
$$

In particular, the lower linear fractional transformation can be given as follows in terms of the weighting transfer functions and closed-loop transfer functions,

$$
\begin{bmatrix} z_s \\ z_t \\ z_u \end{bmatrix} = \begin{bmatrix} W_s S r \\ W_t T r \\ W_u K S r \end{bmatrix} = \begin{bmatrix} W_s S \\ W_t T \\ W_u K S \end{bmatrix} \omega = F_l(P, K)\, \omega \tag{3.31}
$$

The goal of this multi-objective optimization is to minimize the H_∞ norm of the lower linear fractional transformation, $F_l(P, K)$

$$
\|F_l(P, K)\|_\infty = \max_\omega \sigma_{max}(F_l(p, K)(j\omega)) \tag{3.32}
$$

$$
\min_{stab.\,K} \|F_l(P, K)\|_\infty = \min_{stab.\,K} \max_\omega \sigma_{max}(F_l(p, K)(j\omega)) \tag{3.33}
$$

$$
\min_{stab.\,K} \|F_l(P, K)\|_\infty = \min_{stab.\,K} \left\| \begin{bmatrix} W_s S \\ W_t T \\ W_u K S \end{bmatrix} \right\|_\infty \tag{3.34}
$$

As mentioned before designing optimal controller demands large computational effort and is unnecessary. It is a better idea to design a suboptimal controller. Suppose, the minimum value of the H_∞ norm of $F_l(P, K)$ be γ_{min}. Multi-objective optimization using a suboptimal $\gamma > \gamma_{min}$ gives a suboptimal H_∞ controller.

$$
\gamma_{min} = \min_{stab.\,K} \|F_l(P, K)\|_\infty \tag{3.35}
$$

$$
\|F_l(P, K)\|_\infty < \gamma \tag{3.36}
$$

Above equation 3.32 is solved iteratively, where a bisection algorithm is used to choose a value of γ that approaches γ_{min} iteratively, until it is accurate enough based on a predetermined tolerance. In every iteration it is verified that $\gamma > \gamma_{min}$ holds.

MATLAB function *hinfsyn* was used to design the H_∞ controller. The generalized plant, range of γ values, tolerances needs to be provided for the design. This makes the design very convenient.

40

3.3.1　Design

The design objectives of 1 DOF H_∞ controller include:

- All controllers must make the closed-loop robustly stable

- Controllers with large closed-loop bandwidth, ω_b (based on -3 dB crossing of S) needs to be as large as possible

- Controllers with high closed-loop resolution, ω_{bt} (based on -3 dB crossing of T) needs to be as small as possible

- Noise attenuation and disturbance rejection

The fundamental constraints on achieving design objectives:

- $S + T = 1$

- The Bode integral law: $\int_0^\infty log|S(j\omega)|\, d\omega = 0$

- $\omega_b < \omega bt$

Bandwidth is the corresponding frequency of crossing of -3 dB line from below by the sensitivity transfer function S of the closed loop. So, for higher bandwidth it is required that S crosses the -3 dB line at as higher frequency as possible. Also, for disturbance rejection it is required that S has a small value at low frequencies. But, due to the first fundamental constraint T will have to be large in this frequencies to satisfy $S + T = 1$. The Bode integral law states that if the sensitivity transfer function is low at some frequency range then the S will have large values at other frequency ranges. The third fundamental constraint brings in the trade-off between bandwidth and resolution into play. If high bandwidth is targeted then the resolution will be low and vice-versa.

To make S achieve these properties or in other words to give S the proper shape a sensitivity weighting transfer function W_s is designed according to the weight selection criteria described by Skogestad and Poslethwaite [16].

$$W_s(s) = \frac{s/M_p + \omega_{bp}}{s + \omega_{bp}\, m_p} \tag{3.37}$$

$$|S(j\omega)| < 1/|W_p(j\omega)| \quad \forall\, \omega \tag{3.38}$$

$$\leftrightarrow |W_p S| < 1 \quad \forall\, \omega \quad \leftrightarrow \quad \|W_p S\|_\infty < 1 \tag{3.39}$$

Here, $1/|W_s(s)|$ acts as an upper bound for the absolute value of sensitivity transfer function $|S|$. Where, $1/|W_s(s)|$ is equal to $m_p \leqslant 1$ at low frequencies and $M_p \geqslant 1$ at high

frequencies. ω_{bp} is the frequency at which the asymptote of the inverse of the weight i.e. $1/|W_s(s)|$ crosses the magnitude 1 line. ω_{bp} can be taken as the approximate bandwidth requirement in closed-loop. Hence, for a ω_b Hz bandwidth controller a sensitivity weighting transfer function $W_s(s)$ with $\omega_{bp} \leqslant \omega_b$ needs to be designed.
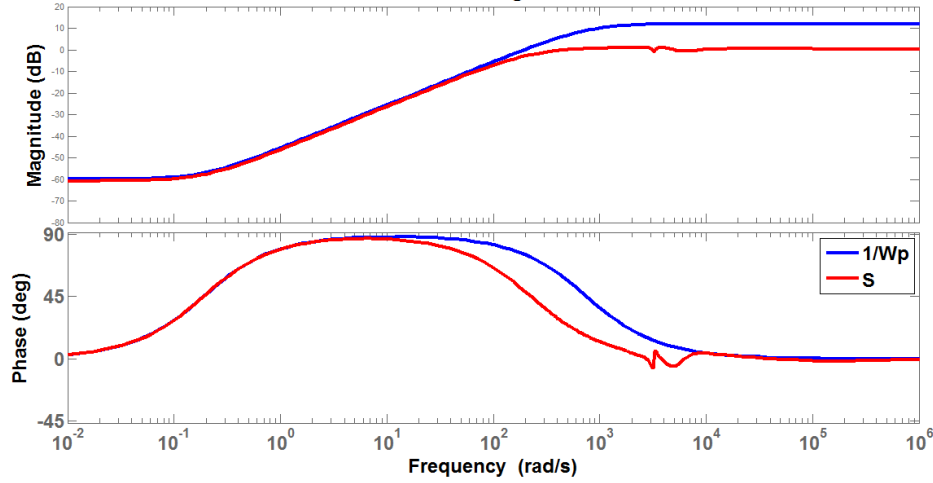

Figure 3.24: Sensitivity transfer function S shaped by the weighting transfer function $1/W_s$. The corresponding H_∞ controller has a bandwidth of 32 Hz, based on -3 dB line crossing by S.

As for example, a $\omega_b = 32$ Hz bandwidth H_∞ controller was designed, with following sensitivity weighting transfer function W_s with $\omega_{bp} = 30$ Hz, low frequency bound $m_p = 1e-3$, and high frequency bound $M_p = 4$, as shown in Figure 3.24. Also from the Figure 3.25 it is clear that the equation 3.39 holds.

$$W_s = \frac{0.25\,s + 188.5}{s + 0.1885} \tag{3.40}$$

For tracking and noise attenuation the complementary sensitivity transfer function T need to be shaped. For noise attenuation at higher frequencies it is required that T has a small value at high frequencies. Good tracking in the region of interest of frequencies requires that the maximum singular value of $T \approx 1$. To give T the proper shape a complementary sensitivity weighting transfer function W_t is designed according to [16].

$$W_t(s) = \frac{s/\omega_{bt} + m_t}{s/\omega_{bt}\,M_t + 1} \tag{3.41}$$

Here, $1/|W_t(s)|$ acts as an upper bound for the absolute value of complementary sensitivity transfer function $|T|$. Where, $1/|W_t(s)|$ is equal to $m_t \leqslant 1$ at low frequencies and $M_t \geqslant 1$ at high frequencies. ω_{bt} is the frequency at which the asymptote of the inverse of the weight
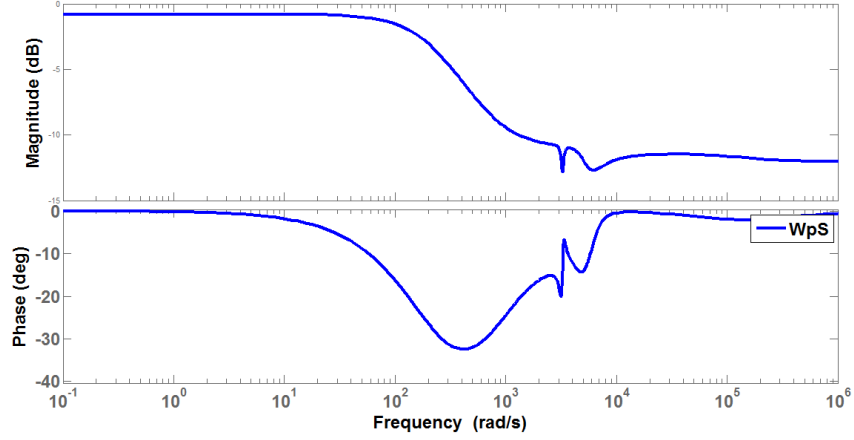
Figure 3.25: Bode of $W_s S$

i.e. $1/|W_t(s)|$ crosses the magnitude 1 line. ω_{bt} can be taken as the approximate bandwidth requirement based on T in closed-loop. Hence, for a ω_b Hz bandwidth (based on S) controller to be designed a complementary sensitivity weighting transfer function $W_t(s)$ with $\omega_{bt} \geqslant \omega_b$ needs to be designed.

$$\omega_{bp} \leqslant \omega_b \leqslant \omega_{bt} \tag{3.42}$$

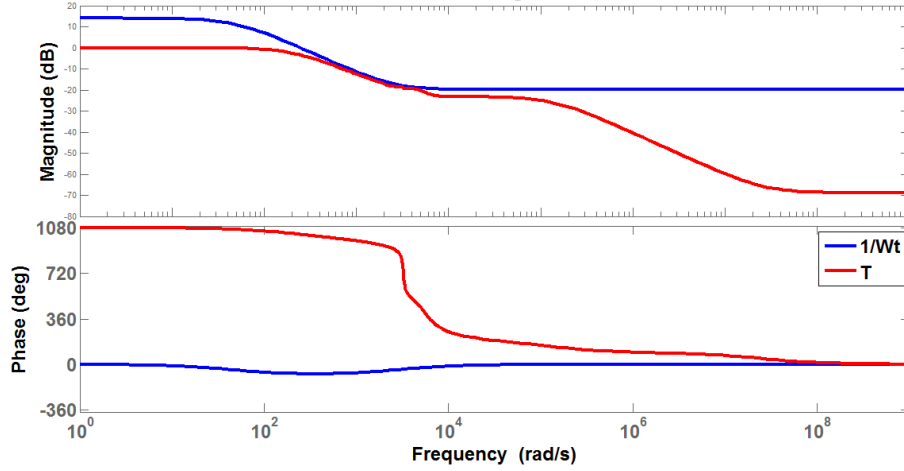Figure 3.26: Complementary sensitivity transfer function T shaped by the weighting transfer function $1/W_t$. The corresponding H_∞ controller has a bandwidth of 32 Hz, based on -3 dB line crossing by S.

As for example, the $\omega_b = 32$ Hz bandwidth H_∞ controller that was mentioned above, with following complementary sensitivity weighting transfer function W_t with $\omega_{bt} = 40$ Hz,

low frequency bound $m_t = 0.2$, and high frequency bound $M_t = 10$, as shown in Figure 3.26.

$$W_t = \frac{0.003979s + 0.2}{0.0003979s + 1} \tag{3.43}$$

With MATLAB function *hinfsyn* the H_∞ controller with 32 Hz bandwidth was designed with a $\gamma = 0.9513$. The maximum bandwidth H_∞ controller designed was 65 Hz. This yields an almost 171% improvement in bandwidth over that of PID controller.

3.3.2   Implementation

The designed continuous-time H_∞ controllers are discretized using the Tustin's method and implemented on EUI fine Y-stage as biquad structures. Controllers up to bandwidth (based on S) of 65 Hz were designed and implemented. That is a 180% improvement in bandwidth over the PID controller. H_∞ controllers having bandwidth 4 Hz, 11 Hz, 28 Hz, 50 hz, and 65 Hz are plotted in a bode plot, as shown in Figure 3.27. In particular the transfer function of 11th order 65 Hz bandwidth controller is given as follows:

$$K_{hinf} = \frac{numtf}{dentf} \tag{3.44}$$

$$
\begin{aligned}
numtf ={}& -2.471e-05s^{11} + 3895s^{10} + 4.171e07s^9 + 1.649e11s^8 + 1.224e15s^7 + 2.065e18s^6 \\
& + 9.313e21s^5 + 8.606e24s^4 + 1.339e28s^3 + 7.606e30s^2 + 2.277e33s + 1.115e36 \\
dentf ={}& s^{11} + 8.473e05s^{10} + 8.903e09s^9 + 5.818e13s^8 + 3.251e17s^7 + 8.85e20s^6 \\
& + 3.061e24s^5 + 3.848e27s^4 + 6.925e30s^3 + 8.034e32s^2 + 1.205e36s + 5.98e35
\end{aligned}
$$

The sensitivity transfer functions of H_∞ controllers having bandwidth 4 Hz, 11 Hz, 28 Hz, 50 hz, and 65 Hz are plotted in a bode plot, as shown in Figure 3.28. As is clear from the definition of the bandwidth, for higher bandwidth the S transfer function should cross the -3 dB line as late as possible.

Now from Table 2.1 it is seen that there are five RHP zeros. Presence of these RHP zeros brings forth the implication of the second waterbed formula [16]. This formula states that if the sensitivity transfer function (S) is pushed down at some frequency range it will rise with high peaks at other frequency range, which is known as the waterbed effect. Visualize the scenario when someone lies down on one side of a waterbed. Obvious result is that the other side of the waterbed would rise. According to the second waterbed formula (Theorem 5.2 in [16]), for closed-loop stability of a system that has real RHP zeros or complex pair of
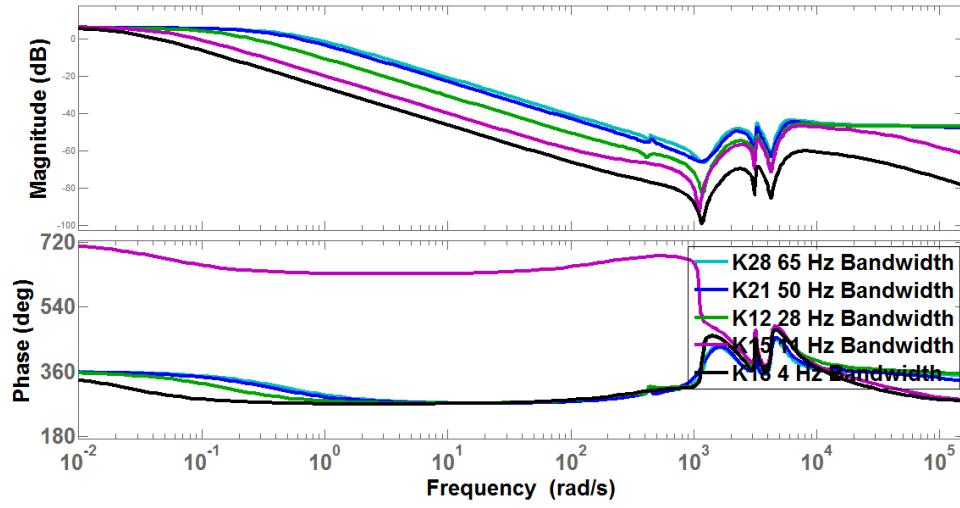
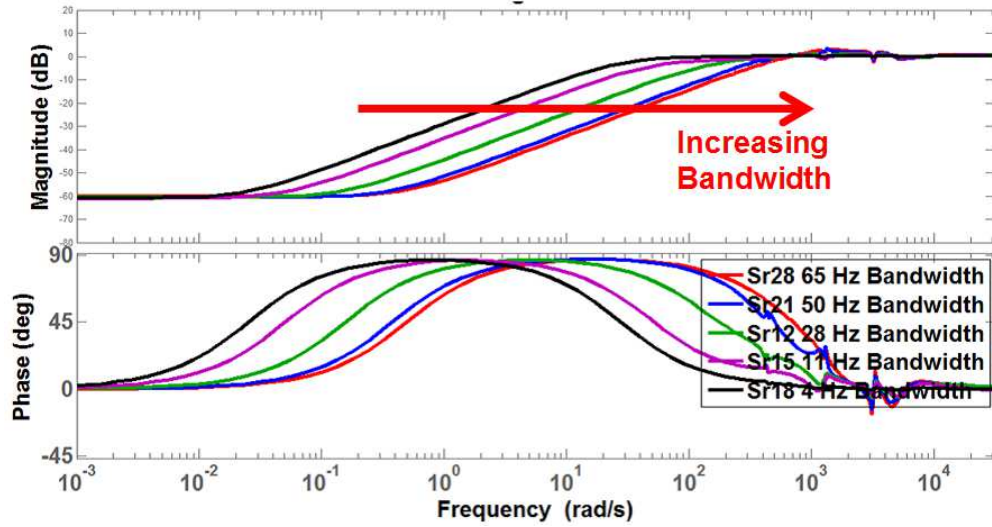Figure 3.27: Comparison of H_∞ controllers of varying bandwidth.

Figure 3.28: Comparison of sensitivity transfer function of H_∞ Controllers of varying bandwidth.

RHP zeros, the sensitivity transfer function S must satisfy the following integral,

$$\int\limits_{0}^{\infty} ln|S(j\omega)|\, w(z,\omega)\, d\omega \;=\; \pi\, ln \prod_{i=1}^{N_p} \left|\frac{p_i + z}{\overline{p_i} - z}\right| \tag{3.45}$$

Where, there are N_p number of RHP poles p_i of loop transfer function $L(s) = G(s)K(s)$, with $\overline{p_i}$ being the complex conjugate of p_i. And z are real or complex pair of RHP zeros of $L(s)$. Here, $w(z,\omega) = \frac{2z}{z^2 + \omega^2}$ for real zero z, and $w(z,\omega) = \frac{x}{x^2 + (y-\omega)^2} + \frac{x}{x^2 + (y+\omega)^2}$ for complex zero pair $z = x \pm jy$.

Figure 3.29 is the magnified version of the Figure 3.28. The waterbed effect or the second waterbed formula is evident in Figure 3.29. For higher bandwidth controllers the sensitivity transfer function needs to be pushed down longer at low frequencies and as a result larger peak at higher frequencies is inevitable. Notice the 50 Hz and 65 Hz controllers have large peaks. If a higher bandwidth controller is designed then the peak of S would cross 5 dB line and the corresponding controller will not be robustly stable any more.
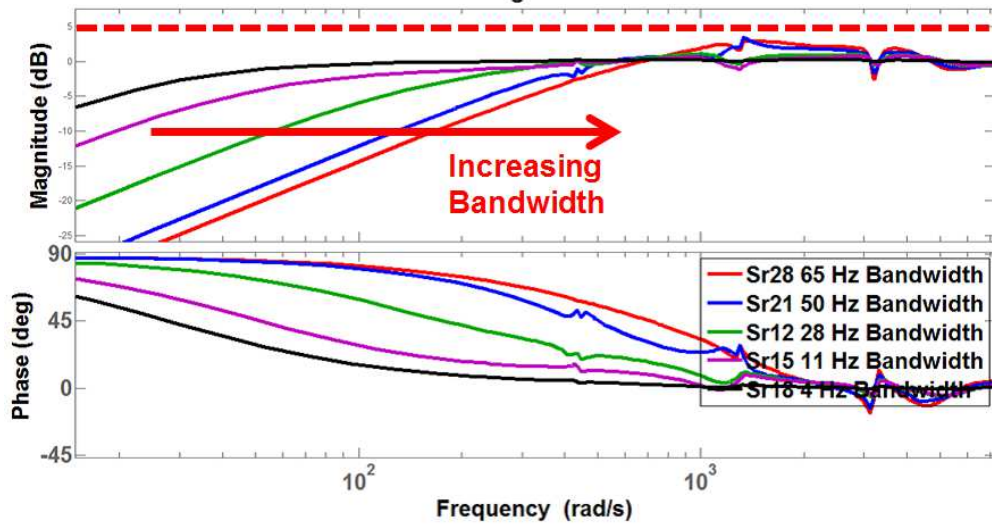

Figure 3.29: Comparison of sensitivity transfer function of H_∞ Controllers of varying bandwidth. With the peak of S for 65 Hz and 50 Hz bandwidth controller being 1.4093 and 1.4825

The closed-loop transfer functions sensitivity transfer function (S), and complementary sensitivity transfer function (T), and , plant transfer function need to be verified. The experimental closed-loop plant model and open loop plant model are closely matched as seen in Figure 3.30. The resonance peaks show that both plants have resonant peak at same frequency. And also the DC value of both plants are also the same. The bode plot of closed-loop sensitivity transfer function (S) and complementary sensitivity transfer function (T)
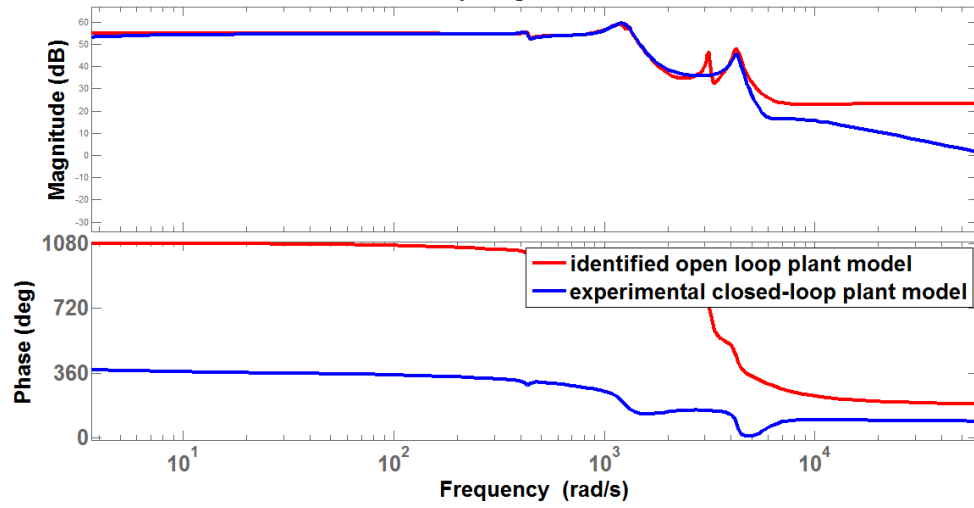
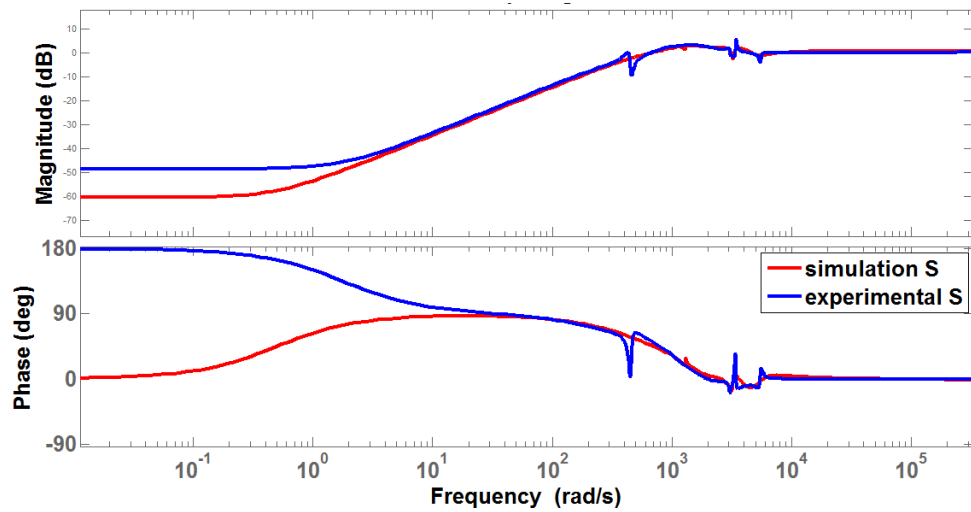Figure 3.30: Bode plot of open loop identified plant model and closed-loop identified plant model.

Figure 3.31: Bode plot of Sensitivity transfer function, S in simulation and experiment.

for simulation and experiment are plotted in the Figure 3.31 and Figure 3.32 respectively. The S and T transfer functions do match well. The bandwidth based on the S transfer function, gives $\omega_{b\,sim} = 65Hz$ and $\omega_{b\,exp} = 56Hz$ for simulation and experimental respectively. The bandwidth based on T transfer function are $\omega_{bt\,sim} = 144Hz$ and $\omega_{bt\,exp} = 175Hz$ for simulation and experimental respectively.
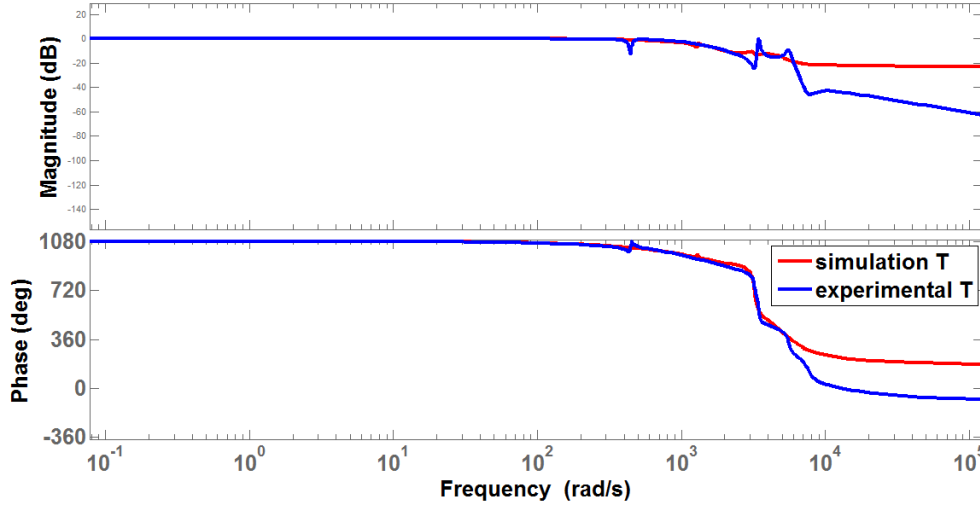

Figure 3.32: Bode plot of Complementary Sensitivity transfer function, T in simulation and experiment.

The bode plot of KS and GS transfer functions for simulation are shown in the Figure 3.33 and Figure 3.34 respectively. The KS transfer function has values well below -40 dB (0.01 in magnitude). So, KS is bounded properly so as to limit the controller output and also to avoid controller saturation. At low frequencies the GS transfer function matches the shape of S and at high frequencies it matches that of the plant transfer functions.

Tracking of triangle wave with 75 nm amplitude and frequencies of 20 Hz and 100 Hz by the 65 Hz bandwidth H_∞ controller is shown in the Figure 3.35. As expected, the H_∞ controller tracks triangular wave better than PID and Glover-McFarlane controllers. Also the output has less offset compared to PID and Glover-McFarlane controllers, as seen in Figure 3.11 and Figure 3.21.

The Figure 3.36 shows the noise-histogram of open loop system output and closed-loop system output based on a 50 Hz H_∞ controller. Clearly the noise-histogram of the closed-loop system output has mean zero and much smaller standard deviation. In other words, small standard deviation means that closed-loop system output data not much dispersed or spread away from the average or zero (which is the mean here). Based on the standard deviation (σ), the $3\sigma-$ resolution of the closed-loop data is 1.4 nm $(3\sigma = 3*0.47)$. Compared to the 7 nm open loop resolution this is almost a 180% improvement in resolution. Also this
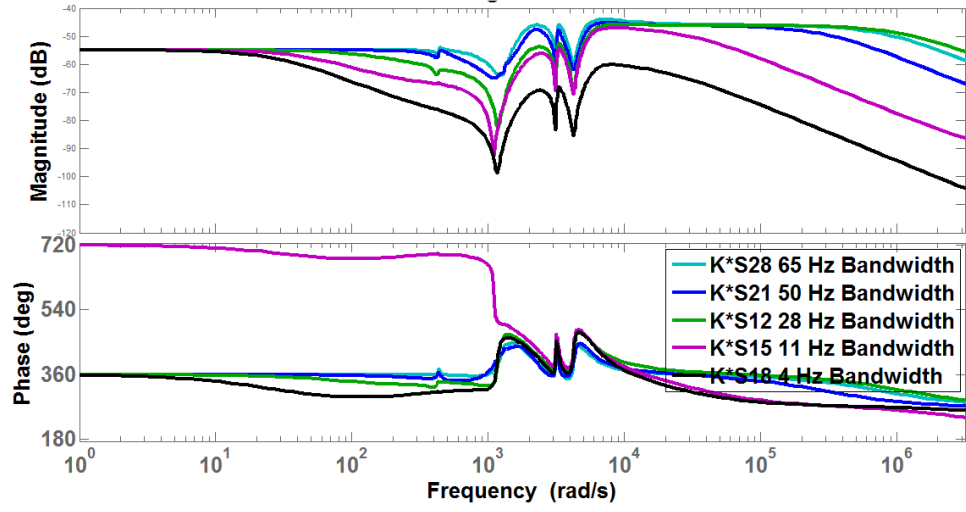
Figure 3.33: Comparison of KS transfer function of H_∞ Controllers of varying bandwidth.
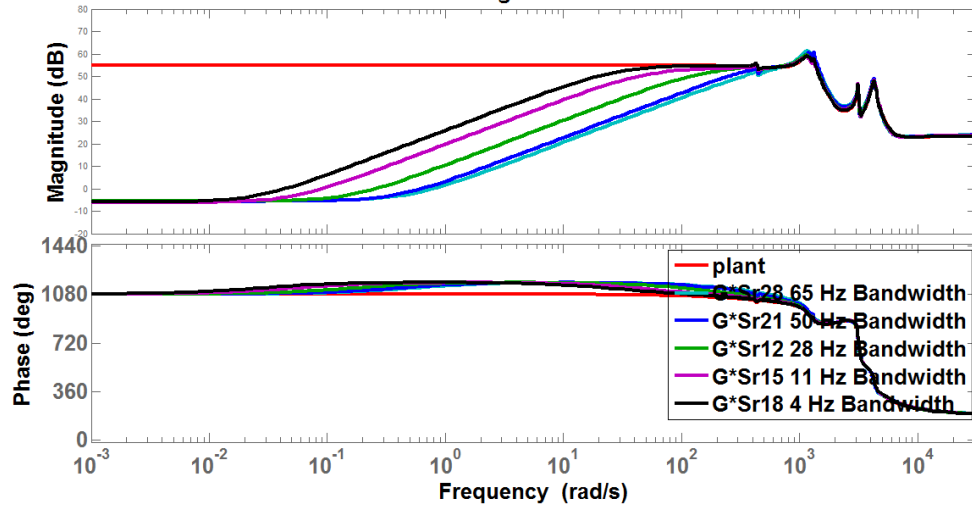
Figure 3.34: Comparison of GS transfer function of H_∞ Controllers of varying bandwidth. The plant G_y is given by the red curve.

(a) 20 Hz Triangle Tracking (b) 100 Hz Triangle Tracking
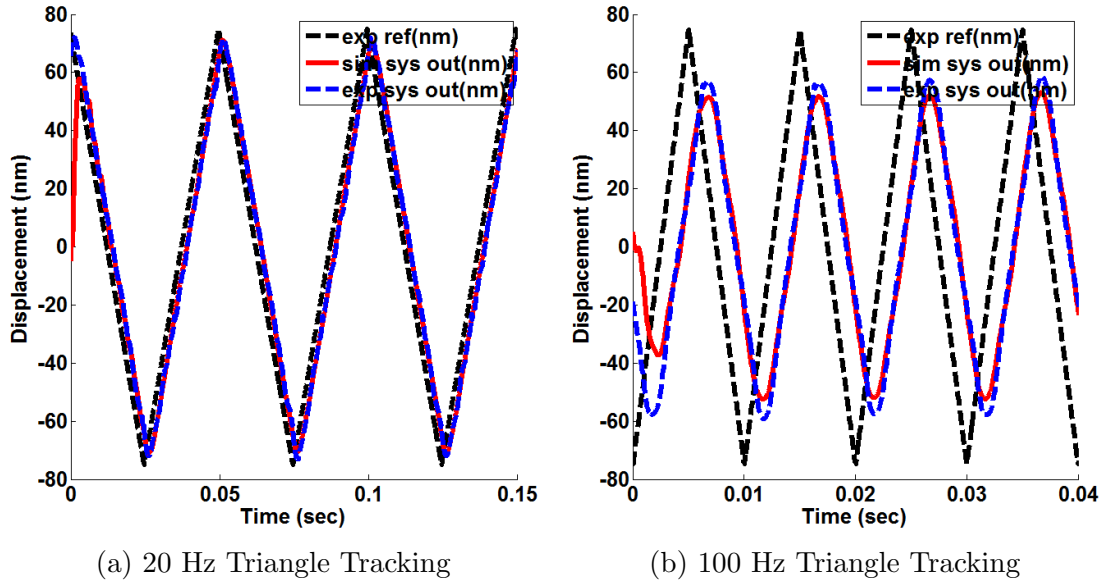
Figure 3.35: Triangular wave tracking verification of 65 Hz bandwidth H_∞ controller.
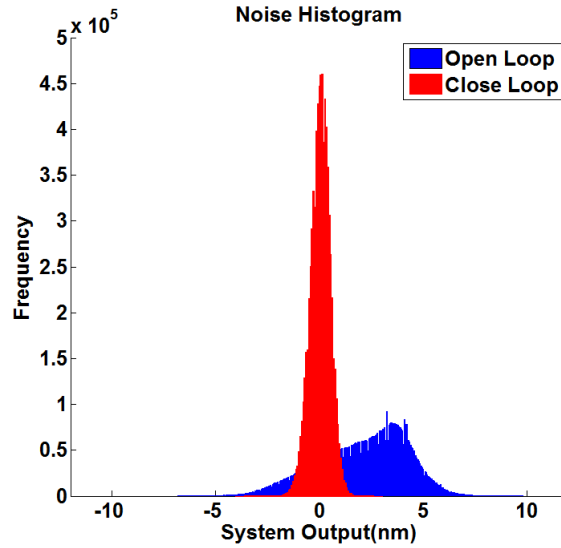
Figure 3.36: Closed-loop noise histogram with a 50 Hz H_∞ controller giving a resolution of approx 1.4 nm. Whereas the open loop resolution is approx 7 nm.

gives resolution improvement of 164% over PID controller and 155% over Glover-McFarlane controller.
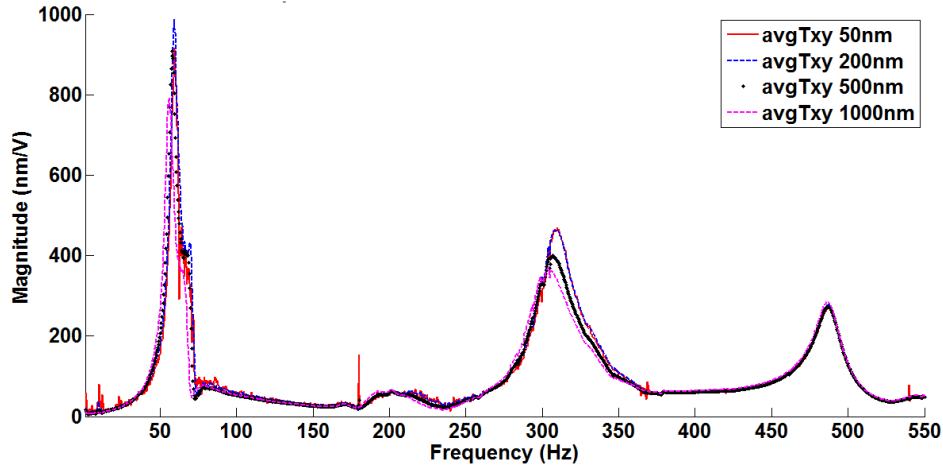
Figure 3.37: Averaged non-parametric transfer functions of the fine XY-stage for 50 nm, 200 nm, 500 nm, 1000 nm input white noise amplitudes. The system exhibits a softening non-linearity.

Given the sufficiently high limits of the sensors and actuators, it was expected that the closed-loop resolution would be better than 1 nm. However this was not the case. Additional factors were explored, among them XY-coupling of EUI stages were one. Figure 3.37 shows the averaged non-parametric transfer function estimation calculated from the time-domain input-output data of XY-stage. Note XY-stage denotes the input-output configuration where input is to the X-stage and the output is measured from the Y-stage. There is a large peak at frequency of 50-60 Hz, which physically means for a small input to the X-stage there is huge output at Y-stage having a frequency of approximately 50-60 Hz due to XY-coupling. The experimental results of Y-stage response also supports this finding. This is likely to be a major factor limiting the resolution of the Y-stage.

CHAPTER 4

CONCLUSION

This thesis describes the design and implementation procedure of different controller algorithms for a nanopositioner used in the X-ray beamline of APS at ANL. The nanopositioner has an optics stage group and a sample stage group, where the optics held on the optics stage group focuses the X-ray beam as a source-size-limited spot on to the sample that is held on the sample stage group. One of fine stages in the optics stage group that moves in the vertical direction (Y-direction) is of main interest for applying controller algorithms. The traditional PID controllers were implemented first because of the ease of design, low order of controller, and ease of implementation. Also PID controllers were considered to be the baseline controllers. PID controllers were designed giving highest bandwidth of 38 Hz and highest resolution of 3.9 nanometers.

The new controller hardware used was National Instruments (NI) CompactRIO hardware that has a real-time controller and a FPGA built in the Hardware chassis. With the dedicated software NI LAbVIEW and controllers running in the FPGA, maximum flexibility of design and implementation is enjoyed. The designed continuous-time controllers are discretized by Tustin's method and represented as biquad structure in the FPGA. The idea of representing the controllers as *second order sections* or *biquads* was a major breakthrough enabling the implementation of controller with any order.

The PID controller in general has very low bandwidth and resolution and also does not make up a robustly stable closed-loop. Controllers that introduce robust stability in the closed-loop system takes care of the uncertainty in the plant model that is being used to design controllers. The Glover-McFarlane robustifying controller is a H_∞ controller that works on a existing industrial controller (say a PID controller) and makes the closed-loop robustly stable. A Glover-McFarlane controller with 38 Hz bandwidth was designed based on a 65 Hz unstable PID controller. Although any higher bandwidth than PID controllers were not possible to design, the Glover-McFarlane controllers were robustly stable. Maximum resolution achieved from EUI applying a Glover-McFarlane controller is 3.1 nanometers, which 155% and 120% improvement over open loop and PID controllers respectively.

Although Glover-McFarlane controller introduced robust stability the corresponding de-

sign procedure is not flexible and the bandwidth achieved is not large. A truly flexible controller algorithm that gives the ease of quantifying trade-offs between performance objectives, assessing if the desired specifications are feasible is the 1 DOF H_∞ controller. Maximum closed-loop bandwidth achieved is 65 Hz, which is 171% improvement over both PID and Glover-McFarlane controllers. The resolution achieved is of 1.4 nm, which are 180%, 164%, and 155% improvements over the open loop, PID controller and Glover-McFarlane controller respectively.

The closed-loop bandwidth is limited due to the presence of RHP zeros in the plant. These RHP zeros through the second waterbed formula acts a limiting factor. In other words the sensitivity transfer function needs to be pushed down up to high frequencies to increase the bandwidth which in turn makes the peak of the sensitivity transfer functions rise higher costing robust stability. The closed-loop resolution was found to be limited by the coupling between the X- and Y-stages. A small noise from the environment going to the X-stage as an input results in large output for the Y-stage specifically at the frequency region of 50-60 Hz, which is verified by independent responses of the plant.

Future work would be to counter the limitations and to improve over the present achievement. A multi-input multi-outptut (MIMO) 1 DOF H_∞ controller design would possibly mitigate the effect of the coupling between the X- and Y-stage, which in turn might improve both the bandwidth and resolution of the X- and Y-stage. Ofcourse, an intermediate step would be to design and implement controllers for X-stage. up to now only true feedback controllers have focused upon. Another approach would be go for a 2 DOF mixed feedforward-feedback H_∞ controller. This 2 DOF controller address both the reference and the plant output in its design algorithm. Additional design criterion conditioning on the reference signal would give better tracking and larger bandwidth.

REFERENCES

[1] Sheikh Mashrafi, Curt Preissner, Srinivasa M. Salapaka, Huyue Zhao, *Something for (Almost) Nothing: X-ray Microscope Performance Enhancement Through Control Architecture Change.* ASPE 28th Annual Meeting, 2013.

[2] J. Maser, B. Lai, T. Buonassisi, Z. Cai, S. Chen, L. Finney, C. Gleber, C. Jacobsen, C. Preissner, C. Roehrig, V. Rose, D. Shu, D. Vine, and S. Vogt, *A Next-Generation Hard X-Ray Nanoprobe Beamline for In Situ Studies of Energy Materials and Devices.* Synchrotron Radiation Instrumentation, Volume 879, pp. 1321-1324, 2013.

[3] Robert P. Winarski, Martin P. Holt, Volker Rose, Peter Fuesz, Dean Carbaugh, Christa Benson, Deming Shu, David Kline, G. Brian Stephenson, Ian McNulty, and Jorg Maser, *A Hard X-ray Nanoprobe Beamline for Nanoscale Microscopy.* Journal of Synchrotron Radiation, Volume 19, pp. 1056-1060, 2012.

[4] Chibum Lee, Srinivasa M. Salapaka, *Robust Broadband Nanopositioning: Fundamental Trade-offs, Analysis, and Design in a Two-Degree-of-Freedom Control Framework.* Nanotechnology, Volume 20, No 3, 2009.

[5] Srinivasa M. Salapaka, Murti V. Salapaka, *Scanning Probe Microscopy.* IEEE Control Systems Magazine, 2008.

[6] D. Shu, J. Maser, M. Holt, R. Winarski, C. Preissner, A. Smolyanitsky, B. Lai, S. Vogt, and G. B. Stephenson, *Optomechanical Design of a Hard X-ray Nanoprobe Instrument with Nanometer Scale Active Vibration Control.* Synchrotron Radiation Instrumentation, Volume 879, pp. 1321-1324, 2007.

[7] D. Shu, J. Maser, B. Lai, S. Vogt, M. Holt, C. Preissner, A. Smolyanitsky, B. Tieman, R. Winarski, and G. B. Stephenson, *Precision Mechanical Design for Hard X-ray Nanoprobe Instrument with Active Vibration Control in Nanometer Scale.* Proceedings of the 8th International Conference on X-ray Microscopy, IPAP Conference Series 7, 2006.

[8] Abu Sebastian, Srinivasa M. Salapaka, *Design Methodologies for Robust Nanopositioning.* IEEE Transactions on Control Systems Technology, Volume 13, No 6, 2005.

[9] D. Shu, J. Maser, M. Holt, B. Lai, S. Vogt, Y. Wang, C. Preissner, Y. Han, B. Tieman, R. Winarski, A. Smolyanitsky, and G. B. Stephenson, *Design and Test of a Differential Scanning Stage System for an X-ray Nanoprobe Instrument.* Optomechanics, Proceedings of SPIE, Volume 5877, 2005.

[10] Srinivasa M. Salapaka, Abu Sebastian, Jason P. Cleaveland, Murti V. Salapaka, *High Bandwidth Nano-Positioner: A Robust Control Approach*. Review of Scientific Instruments, Volume 73, No 9, 2002.

[11] Keith Glover, Duncan McFarlane, *A Loop Shaping Design Procedure Using $H_\infty-$ Synthesis*. IEEE Transactions on Automatic Control, Volume 34, No 8, 1992.

[12] Keith Glover, Duncan McFarlane, *Robust Stabilization of Normalized Coprime Factor Plant Descriptions with $H_\infty-$ Bounded Uncertainty*. IEEE Transactions on Automatic Control, Volume 37, No 6, 1989.

[13] Peter D. Welch, *The Use of Fast Fourier Transform for the Estimation of Power Spectra: a Method based on time Averaging Over short, Modified Periodograms*. IEEE Transactions on Audio and Electroacoustics, Volume AU-15, No 2, 1967.

[14] Karl J. Astrom, Tore Hagglund, *Advanced PID Control*. Instrumentation, Systems, and Automation Society, 2006.

[15] Geir E. Dullerud, Fernando Paganini, *A Course in Robust Control Theory: A Convex Approach*. Springer, Text In Applied Mathematics 36, 2005.

[16] Sigurd Skogestad, Ian Postlethwaite, *Multivariable Feedback Control, Analysis and Design*, John Wiley & Sons, 2nd Edition, 2001.

[17] Sanjit K. Mitra, *Digital Signal Processing - A Computer Based Approach*, McGraw-Hill Series in Electrical and Computer Engineering, 2nd Edition, 2001.

[18] Ashok Ambardar, *Analog and Digital Signal Processing*. McGraw-Hill, 2nd Edition, 1999.

[19] Torsten Soderstrom, Petre Stoica, *System Identification*, Prentice-Hall, 1989.

[20] Lennart Ljung, *System Identification: Theory for the User*, Prentice-Hall, 1987.